

Article

# Davos-Laret Remote Sensing Field Laboratory: 2016/2017 Winter Season L-Band Measurements Data-Processing and Analysis

Reza Naderpour <sup>1,\*</sup> , Mike Schwank <sup>1,2</sup> and Christian Mätzler <sup>2</sup>

<sup>1</sup> Swiss Federal Research Institute WSL, CH-8903 Birmensdorf, Switzerland; mike.schwank@wsl.ch

<sup>2</sup> Gamma Remote Sensing AG, CH-3073 Gümliigen, Switzerland; matzler@gamma-rs.ch

\* Correspondence: reza.naderpour@wsl.ch

Received: 16 October 2017; Accepted: 15 November 2017; Published: 21 November 2017

**Abstract:** The L-band radiometry data and in-situ ground and snow measurements performed during the 2016/2017 winter campaign at the Davos-Laret remote sensing field laboratory are presented and discussed. An improved version of the procedure for the computation of L-band brightness temperatures from ELBARA radiometer raw data is introduced. This procedure includes a thorough explanation of the calibration and filtering including a refined radio frequency interference (RFI) mitigation approach. This new mitigation approach not only performs better than conventional “normality” tests (kurtosis and skewness) but also allows for the quantification of measurement uncertainty introduced by non-thermal noise contributions. The brightness temperatures of natural snow covered areas and areas with a reflector beneath the snow are simulated for varying amounts of snow liquid water content distributed across the snow profile. Both measured and simulated brightness temperatures emanating from natural snow covered areas and areas with a reflector beneath the snow reveal noticeable sensitivity with respect to snow liquid water. This indicates the possibility of estimating snow liquid water using L-band radiometry. It is also shown that distinct daily increases in brightness temperatures measured over the areas with the reflector placed on the ground indicate the onset of the snow melting season, also known as “early-spring snow”.

**Keywords:** L-band radiometry; microwave remote sensing; snow liquid water; LS—MEMLS; ground permittivity; RFI; Davos-Laret

## 1. Introduction

Microwave remote sensing is preeminently suitable to achieve quantitative estimates of large-scale terrestrial state parameters. This is partially due to the high transparency of the atmosphere regardless of weather conditions, particularly within the low-frequency bands of the microwave regime. Furthermore, remote microwave observations do not rely on sunlight, which is decisive to achieve continuous information, especially over the Cryosphere at high latitudes. Another key advantage of microwave remote sensing, over, for example, optical remote sensing, is the significantly larger penetration depth of microwaves in media such as snow [1], vegetation, and soils [2] with moderate amounts of liquid water. However, to retrieve information on terrestrial state-parameters from remotely-measured brightness temperatures, proper microwave emission models are needed, which relate such state parameter values to microwave brightness temperatures. Typically, retrieval approaches involve computationally-expensive iterative procedures employed to optimally fit modeled microwave signatures to the corresponding measurements. Thus, it is important to develop radiative transfer models which not only capture the observed scene’s inherent radiative processes as accurately as possible, but also keep the number of model parameters as low as possible and limited explicitly

to quantities which are accessible from other sources, such as from models or auxiliary remote sensing information.

Nevertheless, the development of radiative transfer models with the aforementioned features necessitates the development and operation of field laboratories allowing for comprehensive, synchronous and collocated in-situ and near-distance remote sensing measurements. Such field laboratories, dedicated to the development of methods to optimally exploit microwave remote sensing of the Cryosphere, are still rare today. Examples of such currently operative research sites include: (i) the Pallas-Sodankylä supersite in Finland [3,4] operated by the Finnish Meteorological Institute Arctic Research Centre (FMI-ARC); (ii) the DOMEX site at Dome-C, Antarctica [5]; (iii) the Kernen Crop Research Farm (KCRF) [6] in Saskatoon operated by the University of Saskatchewan, and (iv) the Maqu regional SMST monitoring network [7]. The most notable example in the Alps is the snow laboratory built on the Weissfluhjoch (2540 m a.s.l., Switzerland) in 1936. Data from this field laboratory include daily records of snow depths and snowfall dating back more than 70 years. During the 1980s, a comprehensive long-term program of microwave-signature studies (summarized in [8]) was conducted at the Weissfluhjoch snow laboratory. This research laid the foundation for the “microwave emission model of layered snowpacks” (MEMLS) [9,10], which is one of today’s widely-used tools to simulate thermal microwave emission of snow [11–16].

Nearly three decades later, the Swiss Federal Research Institute WSL established the Davos-Laret remote sensing field laboratory in 2016 as the only currently-operating Alpine test site dedicated to the development of novel retrieval approaches for the estimation of snow properties from microwave remote sensing data. The present paper provides details on this field laboratory and presents the in-situ data collected during its first operation in Winter 2016/2017 in Sections 2 and 3, respectively. The content is then narrowed to what is relevant for L-band radiometry in the retrieval of snow and ground parameters. In Section 4, we outline the steps taken to achieve calibrated L-band brightness temperatures from ELBARA-II [17] radiometer raw data. This section includes novel approaches to mitigate and filter non-thermal disturbances in ELBARA-II measurements, as well as a method to optimally compensate for thermal noise imposed by transmission losses. With the main purpose being its use for ground-based measurements and validation campaigns, ELBARA-II is designed to have very similar technical specifications to the on-board radiometer of the ESA’s SMOS satellite [18]. Thus, ELBARA-II (and subsequent generations) is used by many research institutes around the world (see for example [7,15,19–21]), indicating that refined data processing methods are beneficial to the passive L-band remote sensing scientific community.

It is worth noting that the penetration depth of L-band microwaves drops from >300 m in dry snow to only a few centimeters for wet snow with ~5% snow liquid water content [22,23]. This, consequently, results in immediate retrieval failure of snow-column properties, or even more so of the underlying ground, as shown in [15,24,25]. Accordingly, as one of the main research questions in the Davos-Laret 2016/2017 winter campaign, the impact of snow liquid water content on L-band brightness temperatures is investigated. Section 5 explains the emission model (Section 5.1) used to analyze the response of simulated brightness temperatures to snow liquid water for snowpacks over “natural ground” and over areas covered with a reflecting metal grid (“reflector areas”—Section 5.2). Afterwards, the temporal and spatial variations of the calibrated L-band brightness temperatures measured over the 2016/2017 winter campaign are presented and discussed. The specific content of Sections 4 and 5 is, on the one hand, valuable on its own, and, on the other hand, preparative for ongoing developments in the retrieval of snow density and ground permittivity [14–16]. In addition, it is of value for the development of a new retrieval approach for the estimation of snow liquid water-column from passive L-band radiometry. The latter two instances are further outlined in Section 6.

## 2. Test-Site Description

The Davos Laret Remote Sensing Field Laboratory (48°50'53" N, 9°52'19" E) in Switzerland is a 50 m × 50 m area with an approximate elevation of 1450 m above sea level. The ground is mostly flat with some smooth slopes on the northwestern side of the site. The valley, including the site area, is surrounded by mountains with an average height difference of ~400 m with respect to the site. The site area is surrounded by Lake Schwarz on the northwestern side, canopy forest on the southeastern side and local buildings on the northeastern and southwestern sides. The spring and summertime vegetation cover of the site is grass.

Dielectric permittivity and temperature of the ground were measured along the two transects shown in Figure 1 using twelve SMT-100 [26] in-situ sensors. Additionally, two SMT-100 sensors were installed on a wooden stick 15- and 50-cm above the ground to measure the permittivity and temperature of the snow at the respective heights (dashed red square in Figure 1). All the sensors were driven with a DT80 data logger which recorded the measured qualities every five minutes. Section 3 presents the time series of these in-situ recordings over the 2016/2017 campaign. In the 2016/2017 Davos Laret campaign, three remote sensing instruments were used:

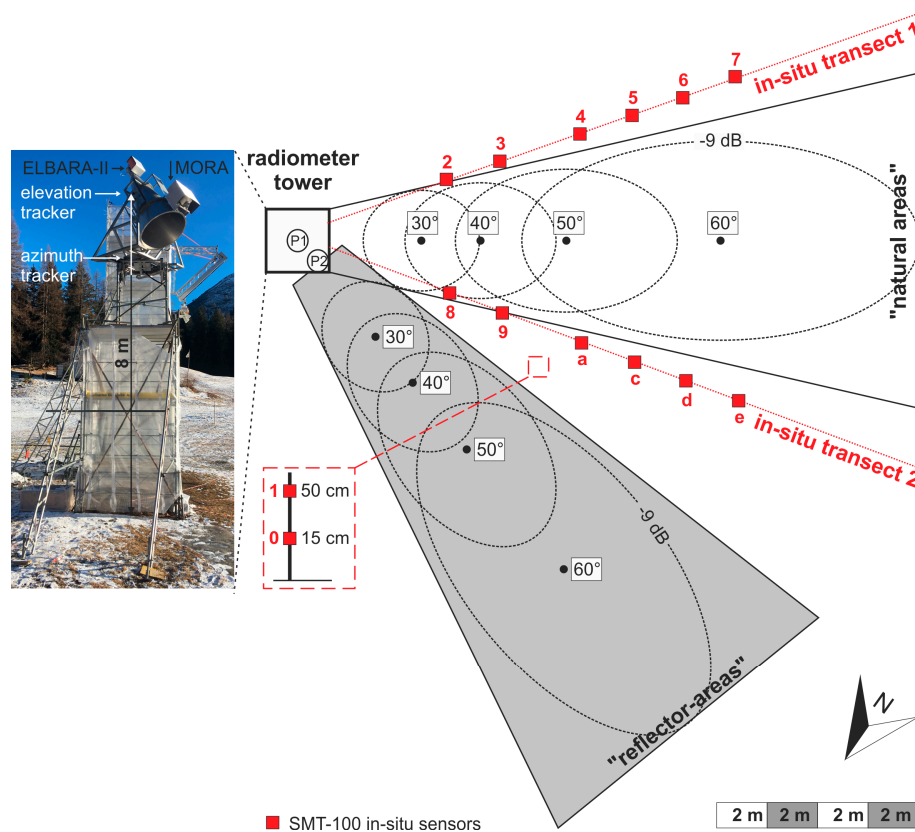


**Figure 1.** Schematics of the footprint areas and the location of the in-situ sensors. ELBARA-II was initially installed at the center (position P1) of the upper-most platform of the tower. The radiometer scaffold was moved to position P2 (bottom right corner of the tower) on 12 December 2016 for RFI improvement.

- The second generation ELBARA-II of the ETH L-band radiometer (ELBARA) operating at horizontal and vertical polarization within the protected part of the L-band (1400–1427 MHz). ELBARA-II technical specifications and its performance under field conditions are outlined by Schwank et al. [17,27]. The first generation ELBARA was designed and constructed in 2001 at the Institute of Applied Physics, University of Bern [28]. A number of ELBARA-II

radiometers were produced by the company Gamma Remote Sensing AG (Gümligen, Switzerland) with the main purpose of calibration and validation activities supporting ESA's SMOS mission [18]. The ELBARA-II assembly, mounted atop an 8-meter tower, includes a tracking system to allow for automated observations of brightness temperatures  $T_B^p(\theta)$  at different nadir angles  $\theta$  and azimuth. For the work presented here, ELBARA-II is the key remote sensing instrument.

- MORA is a single polarization X-band radiometer operating at 11.4 GHz [29]. It is mounted on top of the ELBARA-II antenna (as in [30]) to measure collocated and synchronous X-band brightness temperatures.
- The SnowScat scatterometer is a fully polarimetric, coherent stepped-frequency continuous wave radar operating in the frequency range 9–18 GHz [31]. It is mounted on a rail and attached to a 10-m tower, which allows for elevation and azimuth scanning over the site. Using Synthetic Aperture Radar (SAR) techniques, 3D backscatter maps of the site are made indicating parameters such as radiation penetration depth and snow water equivalent of dry snow.

### 3. In-Situ Measurements

The in-situ measurements performed during the first operation in Winter 2016/2017 of the Davos-Laret field laboratory are presented here, focusing on those used to analyze the collocated and synchronous passive L-band data. Manual in-situ snow-pit characterization (height  $h_S$ , mass-density  $\rho_S$ , and near infrared (NIR) photography) are shown in Section 3.1; automated measurements of ground permittivities  $\epsilon_G$  and temperatures  $T_G$ , as well as snow temperatures  $T_S$ , and meteorological data (air temperatures  $T_{air}$ , precipitation  $r$ ) are shown in Section 3.2.

#### 3.1. Snow Density Profiles

The first major snow fall event during the winter of 2016/2017 occurred on 3 January. During the snow covered period, regular snow-pit measurements were performed manually. Snow height ( $h_S$ ) and mass-density ( $\rho_S$ ) were measured approximately once a week with the first and last measurement on 9 January and 22 March, respectively. A snow cutter was used to measure snow density with a depth resolution of  $\lesssim 10$  cm. The green crosses in Figure 2a,b show measured  $h_S$  and  $\rho_S$ , where the latter represents the average density of the bottom 10 cm of the snowpack derived from the respective profile measurements. Red lines are B-splines fitted to estimate temporal variations of  $h_S$  and  $\rho_S$  in between the times of measurements. The reason for showing snow bottom-layer density  $\rho_S$  is that the snowpack parameter is expected to be the most influential on L-band emission for conditions as explained in [13,14]. Observed  $h_S$  and  $\rho_S$  reveal the expected increasing trend throughout the snow season, while short-term variations are mostly explained by snow metamorphism, settlement, and melting.

With each of the quantitative snow-pit measurements, a NIR image of the snowpack profile was taken to qualitatively track the evolution of the snowpack structure. Figure 3a,b shows the NIR images taken from the newly-formed snowpack on 9 January during the “cold winter period” and the same snowpack and location on 27 February during the “early spring period”, respectively. The most distinct structural features that resulted from snowpack evolution associated with changes in, for example, density and grain size, are marked with dashed green lines. The young snowpack (Figure 3a) has a simple structure with a homogeneous layer in the lowest ~20 cm which was persistent throughout the “cold winter period”. The ~5-cm layer above is less dense, and the fine-grained crisp topmost ~5 cm represents the fresh snow fallen the day before the image was taken. Compared to the young snowpack, the mature snowpack (Figure 3b), nearly two months later, shows almost no clear layering structure. The respective increase in complexity is associated with depth hoar, rounded-snow, and faceted snow formed at the beginning of the “early spring period”. Additionally, the preferential vertical flow paths are signs of liquid water infiltration caused by, for instance, rain or wet snowfall.

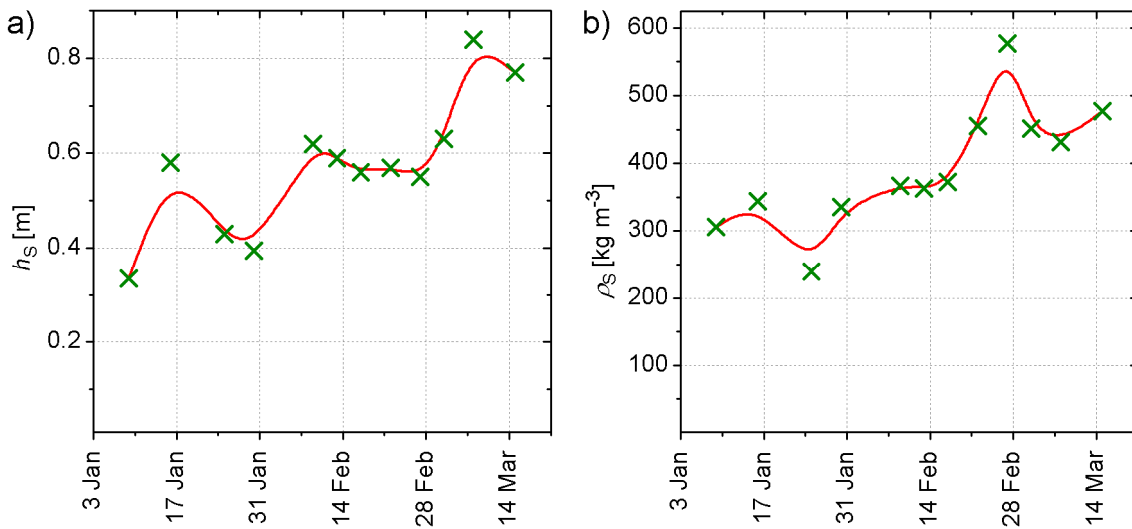


**Figure 2.** (a) Measured snowpack height  $h_s$ ; and (b) average bottom-layer snow density  $\rho_s$  over time. The snow cover quickly melted down in the second half of March 2017 and almost disappeared within approximately the last 10 day of the measurement campaign.

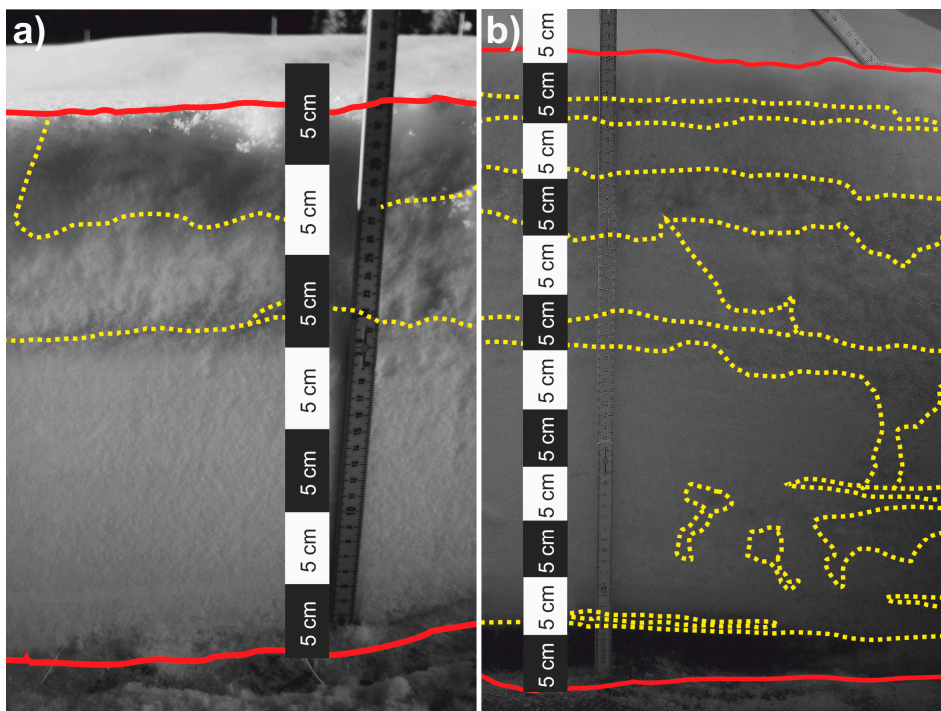


**Figure 3.** NIR photos of the snowpack profile taken on (a) 9 January and (b) 27 February. In addition to an increased snow height, significantly more complex layering and more variable snow grain size and types can be observed in the second profile.

### 3.2. Permittivity, Temperature, and Precipitation

Ground permittivities  $\epsilon_G$  and temperatures  $T_G$  were measured automatically every 5 minutes using SMT-100 sensors [26] installed approximately 5 cm below the ground’s surface. Additionally, two SMT-100 sensors were installed 15 cm and 50 cm above ground to measure either air or snow temperatures  $T_{15\text{ cm}}$  and  $T_{50\text{ cm}}$  depending on snow height  $h_s$  at time of measurement. The thin lines in Figure 4a,b show the time-series of  $\epsilon_G$  from the respective six sensors installed along transects one

and two shown in Figure 1. The thick red line in Figure 4a,b are identical  $\varepsilon_G$  resulting from averaging all twelve ground sensor readings. Likewise, Figure 4c shows  $T_G$  the average of all ground sensor measurements. Figure 4d shows the temperatures  $T_{15\text{ cm}}$  (red),  $T_{50\text{ cm}}$  (green), and  $T_{\text{air}}$  (blue) measured approximately 8 m above the ground by the PT-100 sensor mounted outside the ELBARA-II radiometer. Figure 4e shows precipitation rates  $r$  (for 10-min time windows) for the time period 28 November to 15 March, corresponding to the time period shown for the above in-situ measurements.

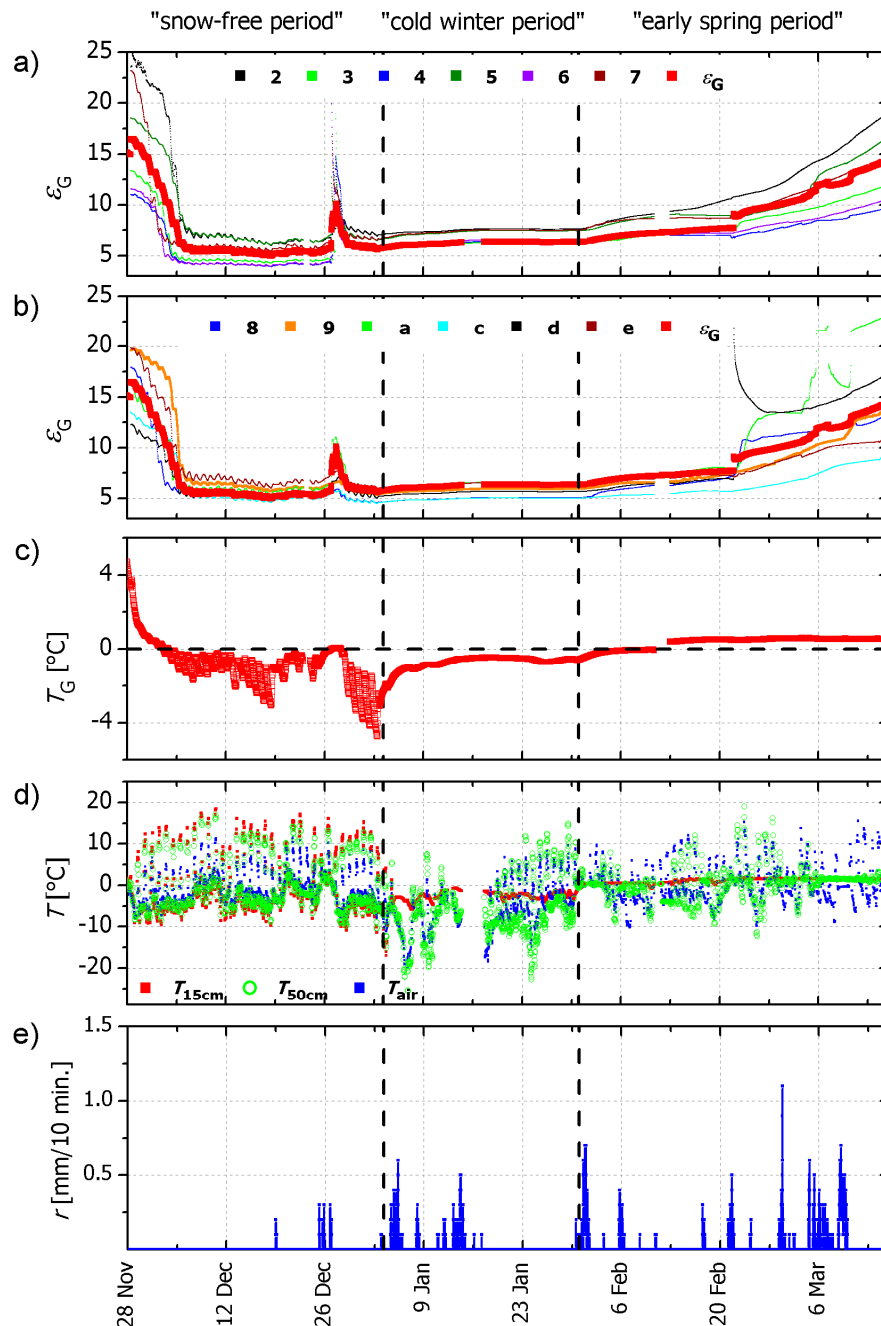


**Figure 4.** Panels (a,b) show the time series of in-situ measured  $\varepsilon_G$  along transects 1 and 2 (shown in Figure 1), respectively. Panel (c) shows the average ground temperature  $T_G$  measured by the 12 SMT-100 sensors along transects 1 and 2. Panel (d) indicates temperatures  $T_{\text{air}}$ ,  $T_{15\text{ cm}}$ , and  $T_{50\text{ cm}}$  measured by ELBARA-II's PT-100 temperature sensor and SMT-100 sensors placed 15 cm and 50 cm above ground, respectively. Panel (e) shows the recorded precipitation (both rain and snow) in units of mm/10 min. over the entire campaign.

The first week of the in-situ time series reveals the rapid freezing of the bare ground surface. This, of course, results from the low diurnal heat input to the ground associated with air temperatures mostly below the freezing point. Figure 4c,d indicate that while during afternoons the temperatures above ground still show short-term peaks above 0 °C, ground temperatures steadily decrease until they fall below the freezing point. However, at the latest by the middle of December, ground permittivities measured by all sensors drop to  $4 \leq \epsilon_G \leq 7$  indicating that at least the top 5 cm of the ground is completely frozen. Around 26 December, a slight thawing event takes place as the result of increased time-integrated heat input and precipitation to the still bare ground. This, in turn, is reflected by  $T_G$  approaching the 0 °C curtain, and finally the increased  $\epsilon_G$  recorded that indicate increased liquid water in the ground surface.

During the “snow-free period” where the ground is frozen, permittivity readings still show small diurnal variations as the result of partial surface melting caused by increased heat input during cloudless afternoons and refreezing overnight. These variations almost completely disappear by 3 January with the onset of snow due to thermal insulation of the accumulating dry snow. The recorded ground permittivities stay at low levels  $4 \leq \epsilon_G \leq 7$  between mid-December and mid-February, indicating that at least the uppermost 5 cm of the ground is frozen during this approximately two-month period.

As shown in Figure 4a,b, in-situ permittivities start increasing gradually after 31 January, indicating that the ground surface starts thawing with the beginning of the “early spring period”. By the middle of March, the ground has almost entirely thawed. Furthermore, deviations between permittivity readings of the different sensors are greater under not-deeply-frozen ground conditions, indicating that heterogeneity of ground permittivity is significantly higher under such transient ground conditions. The most marked example takes place around 21 February, when the readings of sensor d (black symbols in Figure 4b suddenly increase to ~20, while the other sensors along transect 2 react in a much less distinct manner. This distinct heterogeneity in ground permittivity is most likely caused by surface water runoff ponding locally at the position of sensor d.

#### 4. L-Band Radiometry and Raw Data Processing

Brightness temperatures  $T_B^p(\theta)$  measured at given nadir angles  $\theta$  and horizontal ( $p = H$ ) and vertical ( $p = V$ ) polarizations are the basis for successful retrievals based on passive L-band remote sensing. However, calibrated  $T_B^p(\theta)$  are not directly provided by the ELBARA-II radiometer. Instead, they are derived from the instrument’s output data using a radiometer-specific raw-data processing approach. Furthermore, radiometer measurements are sometimes affected by radiative sources other than the natural scene of interest. These perturbing radiation contributions can include man-made Radio Frequency Interferences (RFI) and thermal noise from the surrounding area such as a nearby forest or lake.

Section 4.1 outlines the processing-chain to achieve calibrated  $T_B^p(\theta)$  from ELBARA-II raw-data outputs. Section 4.2 explains and demonstrates an updated RFI mitigation approach. Section 4.3 addresses the issue of computing effective transmission line losses with respect to their time-variability. Finally, the approach used to derive  $T_{B,R}^p(\theta)$  emitted exclusively from the “reflector areas” (see Figure 1) is explained in Section 4.4.

##### 4.1. L-Band Brightness Temperatures

ELBARA-II raw data outputs are voltage samples  $U_i$  consisting of  $i = 1, \dots, nps = 2400$  measurements performed at the sampling rate of 800 Hz during the integration time of 3 s [17]. An ELBARA-II measurement cycle includes the sequential acquisition of voltage samples associated with two internal calibration noise sources (the Active Cold Source (ACS) and the Resistive Source (RS)), and associated with the noise entering the horizontal ( $p = H$ ) and vertical ( $p = V$ ) polarization port of the radiometer assembly (RMA). Each of these voltage samples are recorded for two 11-MHz channels  $ch = 1, 2$  within the protected part (1400–1427 MHz) of the L-band. Accordingly, an ELBARA-II

measurement cycle consists of eight voltage samples  $U_{ACS,i}^{ch}$ ,  $U_{RS,i}^{ch}$ , and  $U_{RMA,i}^{p,ch}$  ultimately used to derive calibrated  $T_B^p(\theta)$ . The processing steps, illustrated in the flowchart in Figure 5 and explained in Sections 4.1.1 and 4.1.2, exclusively use mean values of voltage samples. This is henceforth indicated by omitting the sub-index  $i$ .

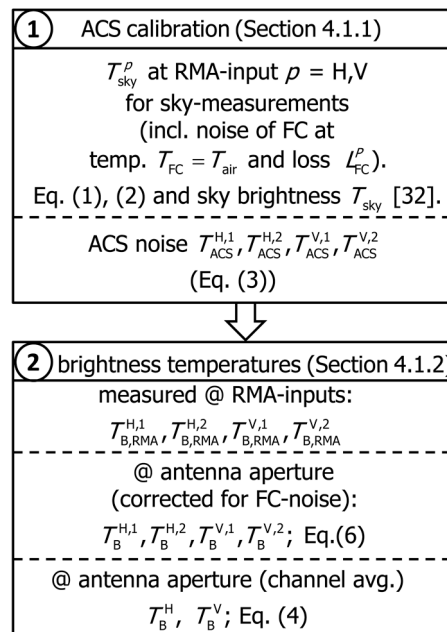


Figure 5. Flowchart of the approach used to convert ELBARA-II raw data into calibrated  $T_B^p$ .

#### 4.1.1. Active Cold Source (ACS) Calibration Using Sky Measurements

The noise temperature  $T_{ACS}^{p,ch}$  of the ACS, implemented in the ELBARA-II radiometer, is calibrated using two noise standards. The accurately known Resistive Source (RS) noise temperature  $T_{RS} = T_{RMA}$  (= actual physical temperature of the interior of the radiometer assembly (RMA)) is one of the noise sources associated with corresponding raw data (voltages)  $U_{RS,i}^{ch}$ , where  $ch = 1, 2$  and  $i = 1, \dots, nps = 2400$ . The second standard noise temperatures are  $T_{RMA}^p = T_{sky}^p$  at the RMA input-ports  $p = H, V$  associated with raw data  $U_{RMA,i}^{p,ch} = U_{sky,i}^{p,ch}$  when pointing the antenna towards the sky at the nadir angle  $\theta = 140^\circ$ . Noise temperatures  $T_{sky}^p = T_{RMA}^p$  (including inherent noise of the transmission line (TL)) are smaller than ACS noise temperatures  $T_{ACS}^{p,ch}$ , which is crucial for the accurate calibration of the ACS. Considering the fact that  $T_{ACS}^{p,ch}$  determined through sky measurements, slightly varies when performed at antenna-port polarization  $p = H, V$ , and also in the two frequency channels  $ch = 1$  and  $2$ , ACS noise temperatures  $T_{ACS}^{H,1}$ ,  $T_{ACS}^{H,2}$ ,  $T_{ACS}^{V,1}$ , and  $T_{ACS}^{V,2}$  are calculated separately for each of the polarization-channel pairs. This is an improvement over the corresponding original ACS calibration approach described in [17] where  $T_{ACS}^{p,ch}$  is assumed to be independent of  $p$  and  $ch$ . It is seen as a pragmatic solution to compensate for impacts of differences in TL losses along the H and V polarization paths (explained in Section 4.3), and differences between the RMA transfer functions of the two frequency channels ( $ch = 1$  and  $2$ ). The rest of this section outlines the procedure used to obtain the four ACS noise temperatures  $T_B^{p,ch}$  ( $ch = 1, 2$  and  $p = H, V$ ), which are used to eventually derive calibrated  $T_B^p$ .

Lossy coaxial transmission lines used to connect the H and V antenna port with the corresponding RMA input ports add their own thermal noise. Consequently, reference noise temperatures

$T_{\text{sky}}^p = T_{\text{RMA}}^p$  at the RMA input  $p = H, V$  are larger than the un-polarized L-band brightness  $T_{\text{sky}} \approx 4.5$  K entering the aperture of the sky-looking antenna:

$$T_{\text{sky}}^p = T_{\text{RMA}}^p = T_{\text{sky}} + (1 - t_{\text{TL}}^p)(T_{\text{TL}} - T_{\text{sky}}) \quad (1)$$

Sky brightness temperature  $T_{\text{sky}}$  entering the aperture of the sky-looking antenna is simulated using the model described in [32,33] for the following parameter values: air humidity  $q_{\text{air}} = 10$  g kg<sup>-1</sup>, rain rate  $r_{\text{air}} = 0$  mm h<sup>-1</sup>, the elevation of the Davos Laret site  $h_{\text{site}} = 1450$  m, the nadir angle  $\theta = 140^\circ$  and  $T_{\text{air}}$  recorded by ELBARA-II at the time of the sky measurement. For  $T_{\text{air}} = 273.15$  K = 0 °C, this yields  $T_{\text{sky}} \approx 4.4$  K. The second summand  $(1 - t_{\text{TL}}^p)(T_{\text{TL}} - T_{\text{sky}})$  in Equation (1) is the noise added by the TLs ( $p = H, V$ ) at common physical temperature  $T_{\text{TL}} = T_{\text{air}}$ . Their power transmission factor  $t_{\text{TL}}^p$  is given by the respective transmission loss  $L_{\text{TL}}^p$  [dB] as:

$$t_{\text{TL}}^p = 10^{-L_{\text{TL}}^p/10} \quad (2)$$

Finally, the four ACS noise temperatures  $T_{\text{ACS}}^{p, ch}$  ( $p = H, V$  and  $ch = 1, 2$ ) are derived from the means  $U_{\text{RS}}^{ch}$ ,  $U_{\text{ACS}}^{ch}$ ,  $U_{\text{sky}}^{p, ch}$  of the voltage samples  $U_{\text{RS}, i}^{ch}$ ,  $U_{\text{ACS}, i}^{ch}$ ,  $U_{\text{RMA}, i}^{p, ch} = U_{\text{sky}, i}^{p, ch}$  and the two reference noise temperatures  $T_{\text{RS}}$  and  $T_{\text{sky}}^p$  as:

$$T_{\text{ACS}}^{p, ch} = \frac{T_{\text{RS}} - T_{\text{sky}}^p}{U_{\text{RS}}^{ch} - U_{\text{sky}}^{p, ch}} (U_{\text{ACS}}^{ch} - U_{\text{sky}}^{p, ch}) + T_{\text{sky}}^p \quad (3)$$

#### 4.1.2. Antenna Brightness Temperatures

Calibrated antenna brightness temperatures  $T_{\text{B}}^p$  ( $p = H, V$ ) measured over ground-areas are derived as the mean of  $T_{\text{B}}^{p, 1}$  and  $T_{\text{B}}^{p, 2}$  at the frequency channels  $ch = 1$  and 2:

$$T_{\text{B}}^p = \frac{T_{\text{B}}^{p, 1} + T_{\text{B}}^{p, 2}}{2} \quad (4)$$

The channel specific  $T_{\text{B}}^{p, ch}$  are expressed by means of noise temperatures  $T_{\text{RMA}}^{p, ch}$  associated with the mean sample voltage  $U_{\text{RMA}}^{p, ch}$  measured for the radiometer pointed towards ground. Again,  $T_{\text{RMA}}^{p, ch}$  at the RMA-input exceed brightness temperatures  $T_{\text{B}}^{p, ch}$  by the amount of inherent noise added by the TL. Therefore, in analogy with Equation (1), they are related via:

$$T_{\text{RMA}}^{p, ch} = T_{\text{B}}^{p, ch} + (1 - t_{\text{TL}}^p)(T_{\text{TL}} - T_{\text{B}}^{p, ch}) \quad (5)$$

Solving Equation (5) for  $T_{\text{B}}^{p, ch}$  immediately yields the channel specific  $T_{\text{B}}^{p, ch}$  corrected by the TL noise as is used in Equation (4):

$$T_{\text{B}}^{p, ch} = \frac{T_{\text{RMA}}^{p, ch} - (1 - t_{\text{TL}}^p)T_{\text{TL}}}{t_{\text{TL}}^p} \quad (6)$$

It should be noted that losses  $L_{\text{TL}}^p$ , used to represent the TLs' inherent noise (second summands in Equations (1) and (5)), can vary in time for a number of reasons such as temperature effects, mechanical stress, and immersive moisture. This can cause both reversible changes in  $L_{\text{TL}}^p$ , as well as irreversible increases in  $L_{\text{TL}}^p$  as the result of ageing. These variations can be taken into account by computing and using the effective  $L_{\text{TL}}^p$  at any given time during the measurement campaign, the method of which is explained in Section 4.3.

Again, in close analogy to Equation (3), the noise temperatures  $T_{\text{RMA}}^{p, ch}$  used in Equation (5) and ultimately used in Equation (4) to derive the calibrated  $T_{\text{B}}^p$ , are computed as:

$$T_{\text{RMA}}^{p, ch} = \frac{\overbrace{T_{\text{RS}} - T_{\text{ACS}}^{p, ch}}^{\equiv S_{\text{RMA}}^{p, ch}}}{U_{\text{RS}}^{ch} - U_{\text{ACS}}^{ch}} (U_{\text{RMA}}^{p, ch} - U_{\text{ACS}}^{ch}) + T_{\text{ACS}}^{p, ch} \quad (7)$$

The radiometer sensitivity  $S_{\text{RMA}}^{p, ch} \approx 0.322 \text{ K} \cdot \text{mV}^{-1}$ , defined above, is almost independent of  $p = \text{H, V}$  and  $ch = 1, 2$ . It will be used as part of the novel Radio Frequency Interference (RFI) mitigation method introduced in Section 4.2 to quantify distortions  $\Delta T_{\text{B}}^{p, ch}$  of  $T_{\text{B}}^p$  caused by non-thermal noise contributions. In addition, as part of the RFI mitigation method, the raw data sample mean  $U_{\text{RMA}}^{p, ch}$  used in Equation (7) is replaced with the mean  $U_{\text{Gauss}}^{p, ch}$  of the Gaussian-model fitted to the probability density function (PDF) of the measured voltage sample  $U_{\text{RMA}, i}^{p, ch}$ .

#### 4.2. Radio Frequency Interference Detection and Mitigation

RFI can be defined as any electromagnetic signal, other than thermal noise emitted from within the antenna footprint, contributing to the measured antenna brightness temperature  $T_{\text{B}}^p$ . Man-made RFI sources include spurious signals from other frequency bands, spread-spectrum signals overlapping the “protected” band of operation, or out-of-band emissions not properly rejected by the pre-detection filters [34]. The statistical distribution of a measured sample  $U_{\text{RMA}, i}^{p, ch}$  performed on a perfectly undisturbed thermal noise source should theoretically match a Gaussian probability density function  $\text{PDF}_{\text{Gauss}}$ , whereas its standard deviation results from the uncertainties of the individual  $U_{\text{RMA}, i}^{p, ch}$  determined by the time-bandwidth product (see Section 3.2 in [17]).

Using RFI corrupted  $T_{\text{B}}^p$  in remote sensing results in erroneous retrievals [35–37]. Thus, it is critically important to mitigate, or at least detect, RFI in passive microwave remote sensing. RFI detection methods used most often are essentially statistical “normality” tests which quantify the non-Gaussianity of measured sample distributions by means of using thresholds for associated Kurtosis and Skewness [34]. Among the more sophisticated algorithms are the “Kolmogorov-Smirnov” (KS) method [38] and the Lilliefors (L) normality test [39]. However, the former can often wrongly estimate the mean and variance of the normal distribution and the latter has limitations in that it tends to be more sensitive at the center than near the tail of the distribution.

Widely used “normality” tests (based on Kurtosis and Skewness), were initially tried on our ELBARA-II data to detect RFI. However, as also reported in [40–43], these simple approaches often failed even for physically meaningless measurements  $T_{\text{B}}^{p, ch}$ . Consequently, we use a more rigorous normality test which not only identifies RFI, but also quantifies the extent to which non-thermal distortion  $\Delta T_{\text{B}}^{p, ch}$  affects  $T_{\text{B}}^{p, ch}$ . Quantitative estimates of distortions become valuable especially when radiometer measurements of  $T_{\text{B}}^{p, ch}$  are used in retrieval schemes because it allows to assign less weight to  $T_{\text{B}}^{p, ch}$  in accordance with its non-thermal distortion  $\Delta T_{\text{B}}^{p, ch}$ .

The RFI mitigation approach used here consists of the following steps. Firstly, the probability density function  $\text{PDF}_{\text{m}}(U_{\text{RMA}, i}^{p, ch})$  associated with the measured (m) raw-data voltage sample  $U_{\text{RMA}, i}^{p, ch}$  is computed numerically. Secondly, the measurement based  $\text{PDF}_{\text{m}}(U_{\text{RMA}, i}^{p, ch})$  is approximated with a Gaussian model  $\text{PDF}_{\text{Gauss}}(U_{\text{RMA}, i}^{p, ch})$  including the parameters  $\hat{U}_{\text{Gauss}}^{p, ch}$ ,  $U_{\text{Gauss}}^{p, ch}$ ,  $\sigma_{\text{Gauss}}^{p, ch}$  to represent optimized values of its peak, mean, and standard deviation, respectively:

$$\text{PDF}_{\text{Gauss}}(U_{\text{RMA}, i}^{p, ch}) = \hat{U}_{\text{Gauss}}^{p, ch} \cdot \exp\left(\frac{-\left(U_{\text{RMA}, i}^{p, ch} - U_{\text{Gauss}}^{p, ch}\right)^2}{2 \cdot \sigma_{\text{Gauss}}^{p, ch}}\right) \quad (8)$$

To achieve high sensitivity to residuals in the fit of  $PDF_{\text{Gauss}}(U_{\text{RMA},i}^{p,ch})$  with respect to underlying measured  $PDF_{\text{m}}(U_{\text{RMA},i}^{p,ch})$ , the following conditions are imposed on the numerical optimization:

- The starting value of  $U_{\text{Gauss}}^{p,ch}$  is set to the mean  $U_{\text{RMA}}^{p,ch}$  of the measured sample  $U_{\text{RMA},i}^{p,ch}$ .
- The codomain of  $U_{\text{Gauss}}^{p,ch}$  is restricted by the lowest measurement to  $U_{\text{Gauss}}^{p,ch} \geq \min(U_{\text{RMA}}^{p,ch})$
- The starting value of  $\sigma_{\text{Gauss}}^{p,ch}$  is set to 0.02 mV corresponding to the typical standard deviation of a sample  $U_{\text{RS},i}^{ch}$  measured on the resistive noise source.
- The codomain of  $\hat{U}_{\text{Gauss}}^{p,ch}$  is restricted to  $\hat{U}_{\text{Gauss}}^{p,ch} \geq 20$

In the third step, the coefficient of determination  $R^2$  between  $PDF_{\text{m}}(U_{\text{RMA},i}^{p,ch})$  and  $PDF_{\text{Gauss}}(U_{\text{RMA},i}^{p,ch})$  is computed to quantify the Gaussianity of the statistics of a measured sample  $U_{\text{RMA},i}^{p,ch}$ . Fourth, the threshold  $R^2 < 0.95$  is applied to flag the sample  $U_{\text{RMA},i}^{p,ch}$  for exclusion from further analysis due to RFI. Upon successful Gaussian fitting ( $R^2 \geq 0.95$ ), the optimized mean value  $U_{\text{Gauss}}^{p,ch}$  of  $PDF_{\text{Gauss}}(U_{\text{RMA},i}^{p,ch})$  is used to compute  $T_{\text{B}}^{p,ch}$  (using Equation (7)) instead of the mean  $U_{\text{RMA}}^{p,ch}$  of the measured sample  $U_{\text{RMA},i}^{p,ch}$ .

The fifth step is the quantification of the distortion imposed by non-thermal RFI on the measurement of  $T_{\text{B}}^{p,ch}$ . The resulting measurement error  $\Delta T_{\text{B}}^{p,ch}$  is estimated as:

$$\Delta T_{\text{B}}^{p,ch} = \left| U_{\text{Gauss}}^{p,ch} - U_{\text{RMA}}^{p,ch} \right| \cdot S_{\text{RMA}} \quad (9)$$

Thereby, radiometer sensitivity  $S_{\text{RMA}}^{p,ch} \approx 0.322 \text{ K}\cdot\text{mV}^{-1}$  (defined in Equation (7)) is used to “translate” the difference between the mean voltages  $U_{\text{RMA}}^{p,ch}$  and  $U_{\text{Gauss}}^{p,ch}$  of the measured sample  $U_{\text{RMA},i}^{p,ch}$  and the fitted  $PDF_{\text{Gauss}}$  to the difference  $\Delta T_{\text{B}}^{p,ch}$  between brightness temperatures. The usefulness of the measurement uncertainty factor  $\Delta T_{\text{B}}^{p,ch}$  lies in its application in retrievals based on L-band radiometry (such as in [14–16]) where  $T_{\text{B}}^{p,ch}$  can be weighted according to their non-thermal distortion levels. This essentially indicates that less influence on the retrieval results occurs from more disturbed measurements.

Figure 6 shows representative examples of PDFs associated with measured voltage samples  $U_{\text{RMA},i}^{p,ch}$  ( $p = V$ , and  $ch = 1$ ) including different levels of non-thermal RFI. Blue lines are  $PDF_{\text{m}}(U_{\text{RMA},i}^{V,1})$  derived from measured samples  $U_{\text{RMA},i}^{V,1}$ , red lines represent the Gaussian model  $PDF_{\text{Gauss}}(U_{\text{RMA},i}^{V,1})$  fitted to the measurement based  $PDF_{\text{m}}(U_{\text{RMA},i}^{V,1})$ . Figure 6a shows the case of an almost RFI-free sample, for which  $PDF_{\text{m}}(U_{\text{RMA},i}^{V,1})$  and  $PDF_{\text{Gauss}}(U_{\text{RMA},i}^{V,1})$  match well. Accordingly, the coefficient of determination  $R^2 = 0.99$  is high, and the non-thermal contribution  $\Delta T_{\text{B}}^{V,1} = 0.66 \text{ K}$  is minor. Likewise, Kurtosis  $K = 2.77$  and Skewness  $S = 0.35$  indicate an almost RFI-free sample. Figure 6b shows an example of a distorted sample, which would not necessarily be recognized by simply looking at Kurtosis  $K = 3.06$  and Skewness  $S = 0.46$  values. However, the non-Gaussianity of  $PDF_{\text{m}}(U_{\text{RMA},i}^{V,1})$  is obvious and becomes apparent in the reduced  $R^2 = 0.64$  (RFI-flag is raised), and the significant RFI-distortion  $\Delta T_{\text{B}}^{V,1} = 1.21 \text{ K}$ . The PDFs shown in Figure 6c,d are examples of heavily RFI distorted measurements. As a consequence of the imposed conditions (indicated in the bullet points above) the Gaussian fits  $PDF_{\text{Gauss}}(U_{\text{RMA},i}^{V,1})$  clearly fail, yielding  $R^2 = 0.0$  in both cases. The RFI distortion shown in Figure 6c would also have been detected by means of the statistical moments  $K = 5.16$  and  $S = 1.19$ . However, the example in Figure 6d would not necessarily be rejected as RFI-distorted based on  $K = 2.29$  and  $S = 0.03$  given their assumed thresholds of around 3.0 and 0.0, respectively.

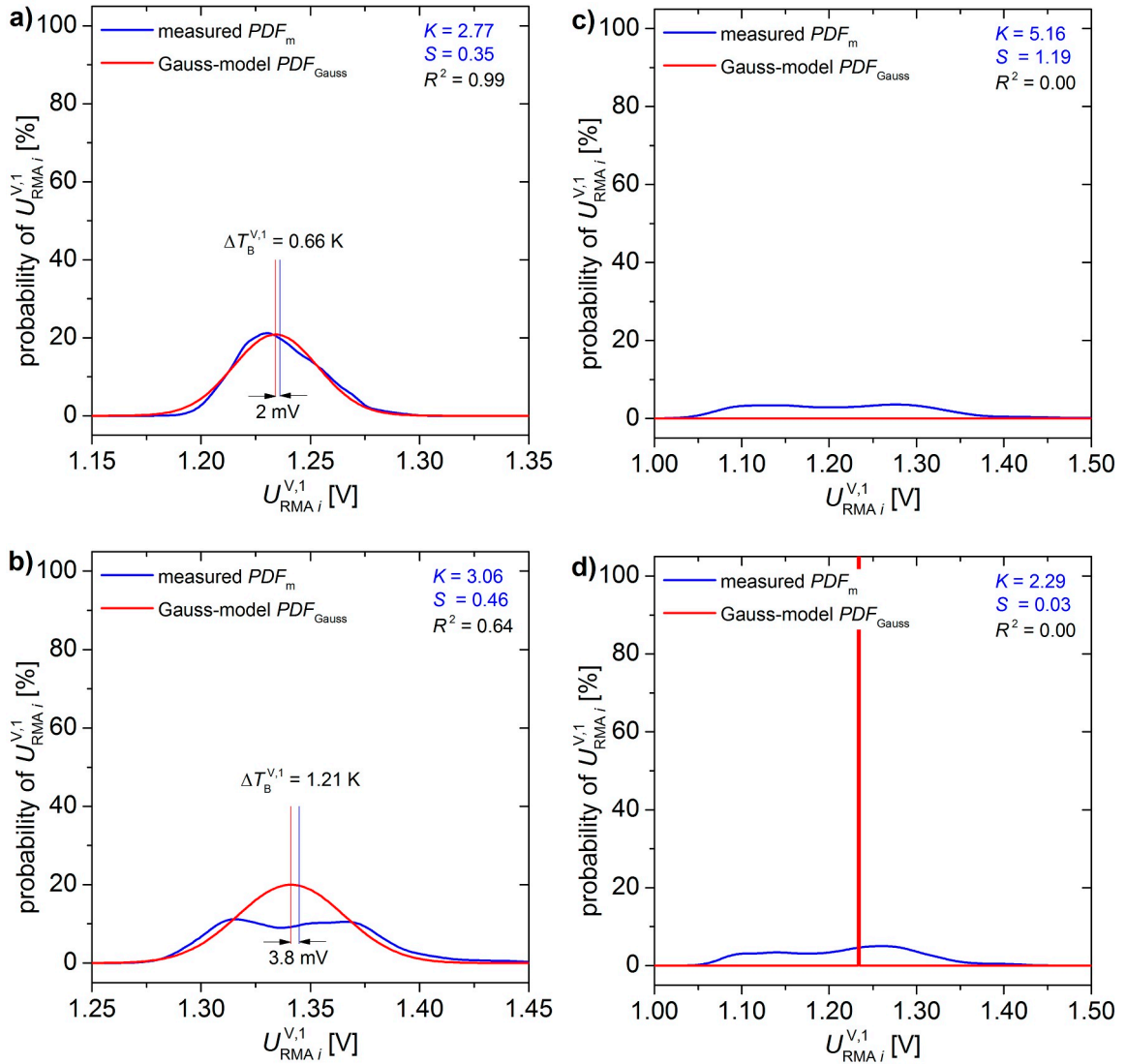


**Figure 6.** Four examples of measured sample voltage distributions  $PDF_m(U_{RMA,i}^{V,1})$ , and the corresponding Gaussian fits  $PDF_{Gauss}(U_{RMA,i}^{V,1})$ : (a) a “healthy” measurement; and (b–d) distorted measurements.

#### 4.3. Effective Transmission Losses and ACS Temperatures

As explained earlier,  $T_B^p$  corresponds with the noise  $T_{B,RMA}^p$  at the RMA-inputs  $p = H, V$  reduced by the transmission lines’ inherent noise (Equation (6)). Because transmission line (TL) noise depends on its physical temperature  $T_{TL}$  and on its loss  $L_{TL}^p$ , the use of an “effective” value of  $L_{TL}^p$  is necessary to optimally minimize distortions of  $T_B^p$  imposed by temporal variations of  $T_{TL}$ . The approach developed to achieve effective  $L_{TL}^{p*}$  and optimal ACS noise-temperatures  $T_{ACS}^{p,ch*}$  is outlined in the flowchart shown in Figure 7. This approach is based on the assumption that TL losses are optimally chosen if, for a range of TL-temperatures  $T_{TL} = T_{air}$ , deviations between theoretical sky-brightness and measurement-based  $T_{sky}^p$  are minimal.

Sky measurements were performed regularly throughout the campaign between 28 November and 3 March by pointing the radiometer skyward at nadir angle  $\theta = 140^\circ$  ( $= 40^\circ$  relative to zenith). This resulted in  $N_{sky} = 88$  measurement cycles, each of which consists of 8 undisturbed voltage samples  $U_{ACS,i}^{ch}$ ,  $U_{RS,i}^{ch}$  and  $U_{RMA,i}^{p,ch}$  ( $i = 1, \dots, nps = 2400$ ) and covers the temperature range of  $-20^\circ C \leq T_{air} = T_{TL} \leq 14^\circ C$ . To begin with, the first  $N_0 = 50$  sample-means  $U_{ACS}^{ch}$ ,  $U_{RS}^{ch}$  and  $U_{RMA}^{p,ch}$  (28 November–11 January) with associated measurements  $T_{TL} = T_{air}$  were used together with initial

guesses  $L_{TL}^{p, ini}$  of transmission lines to compute the associated ACS temperatures  $T_{ACS}^{p, ch}$  (Section 4.1.1). From these  $N_0$  foursomes of  $T_{ACS}^{p, ch}$ , the corresponding four temporal mean values  $\langle T_{ACS}^{p, ch} \rangle$  were computed as illustrated in Boxes 1–3 in the flowchart (Figure 7). Next, the four mean values  $\langle T_{ACS}^{H,1} \rangle$ ,  $\langle T_{ACS}^{H,2} \rangle$ ,  $\langle T_{ACS}^{V,1} \rangle$ , and  $\langle T_{ACS}^{V,2} \rangle$  were used to compute the four time-series  $T_{sky}^{H,1,j}$ ,  $T_{sky}^{H,2,j}$ ,  $T_{sky}^{V,1,j}$ , and  $T_{sky}^{V,2,j}$  (using Equation (6) with Equation (7)) based on the voltage sample-means recorded for the first  $j = 1, \dots, N_0 + k$  sky measurements. Furthermore, synchronous theoretical time series  $T_{sky}^j$  were simulated using [32] (Box 4 in the flow-chart). Naturally, the measurement-based time-series  $T_{sky}^{p, ch, j}$  do not perfectly agree with the simulated  $T_{sky}^j$ , and result in a Root-Mean-Square Error  $RMSE(T_{sky}^p)$ , defined in Box 5 of the flow chart.

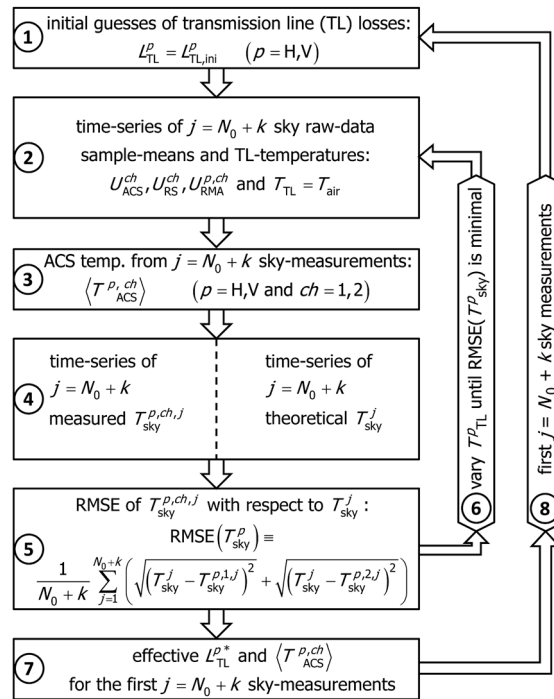


**Figure 7.** Flowchart illustrating the course of action followed to estimate effective losses of transmission line (TL) and active cold source (ACS) noise temperatures.

The magnitude of  $RMSE(T_{sky}^p)$  depends on the assumption made regarding  $L_{TL}^p$  because it determines the degree to which fluctuations in  $T_{TL} = T_{air}$  translate into fluctuations of  $T_{sky}^{p, ch, j}$ . An excessively high value of  $L_{TL}^p$  causes  $T_{sky}^{p, ch, j}$  that are distorted by overcompensation of temperature-dependent TL-noise. An excessively low value of  $L_{TL}^p$  leads to an underestimation of this effect. Accordingly, the computation of effective TL-losses  $L_{TL}^{p, *}$  and ACS temperatures  $\langle T_{ACS}^{p, ch} \rangle$  for a given time period (including  $j$  sky measurements) consists of iterating Steps 2–5 (Loop 6 in the flow chart) until  $RMSE(T_{sky}^p)$  becomes minimal (Box 7). As indicated above, the initial period, consisting of the first  $N_0 = 50$  sky measurements, is used to compute  $L_{TL}^{p, *}$  and  $\langle T_{ACS}^{p, ch} \rangle$  representative of this training period, and ultimately applied to derive  $T_B^p$  of footprint areas for this period. For later time periods,  $T_B^p$  are derived from effective values  $L_{TL}^{p, *}$  and  $\langle T_{ACS}^{p, ch} \rangle$  estimated from the growing number  $j = 1, \dots, N_0 + k$  of sky measurements as indicated by the outermost Loop 8 in the flowchart shown in Figure 7.

Figure 8a shows the increasing trend of  $L_{TL}^{p, *}$  over time for both polarizations ( $p = H, V$ ). This can be explained, for instance, by ageing and the accumulation of moisture in the TL-connectors as well as the  $\lambda/4$  dipoles within the Picket-horn antenna [17]. Throughout the entire campaign a total

increase of about 0.08 dB and 0.21 dB is observed for  $L_{TL}^{H*}$  and  $L_{TL}^{V*}$ , respectively. After 23 January, the  $L_{TL}^{H*}$  values almost saturate to 0.43 dB whilst  $L_{TL}^{V*}$  continues increasing until the end of the campaign. The systematically larger  $L_{TL}^{V*}$ , in comparison to  $L_{TL}^{H*}$ , is consistent with the smaller bending radius of the V-polarization TL, compared to the H-polarization TL. This is because the  $\lambda/4$  dipole receiving vertical polarized radiance is mounted at the very back of the antenna-feed (see Figure 4 in [17]). Beyond this, the V-polarization  $\lambda/4$  dipole is more susceptible to contaminations because of its mounting position.

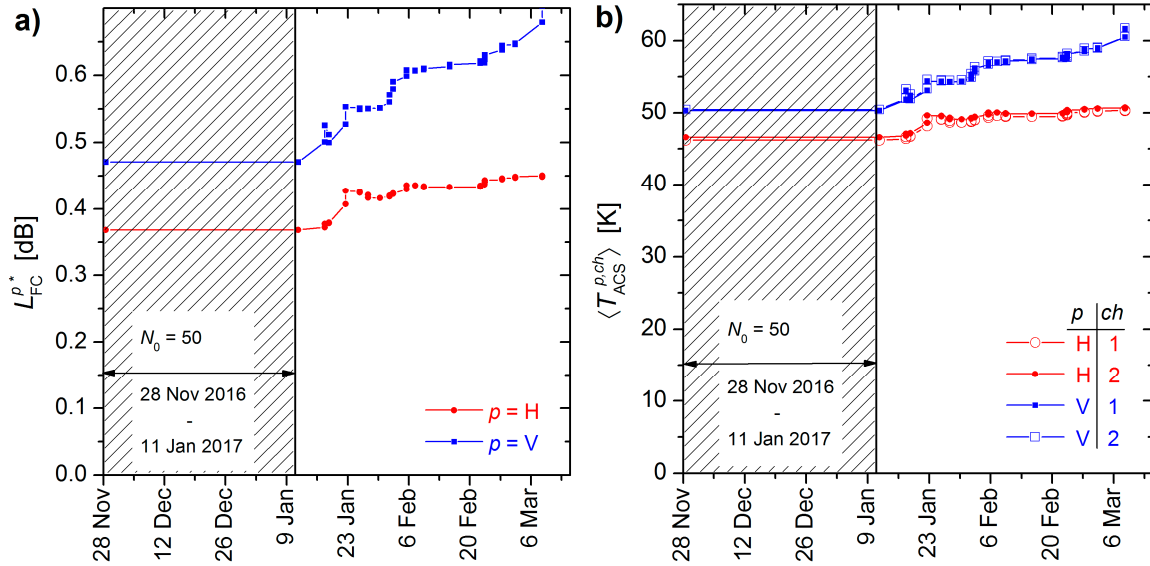


**Figure 8.** (a) Effective  $L_{TL}^{p*}$  and (b)  $\langle T_{ACS}^{p,ch} \rangle$  ( $ch = 1, 2$  and  $p = H, V$ ) computed with increasing numbers of sky measurements.

Figure 8b shows similar increasing trends for the four ACS noise temperatures  $\langle T_{ACS}^{p,ch} \rangle$  ( $p = H, V$ ;  $ch = 1, 2$ ) computed as the temporal mean of the first  $j = 1, \dots, N_0 + k$  individual ACS temperatures  $T_{ACS}^{p,ch}$ . This increase, however, is a direct consequence of increasing  $L_{TL}^{p*}$  as can be seen when calculating Equations (1)–(3) for increasing  $L_{TL}^{p*}$ . It was verified that the sample-means  $U_{ACS}^{ch}$  do not increase throughout the campaign. This confirms that increasing  $\langle T_{ACS}^{p,ch} \rangle$  are not due to increasing noise power of the RMA internal ACS, but indeed results from ACS calibration based on sky measurements  $U_{RMA}^{p,ch} = U_{sky}^{p,ch}$  which increase with increasing TL losses.

#### 4.4. Brightness Temperatures of “Reflector Areas”

Brightness temperatures  $T_{B,R}^p$  originating exclusively from the areas with the metal-mesh reflector beneath the snow (“reflector areas” shown in Figure 1) are useful to investigate snow emission segregated from ground emission. This is important, for instance, when investigating impacts of snow liquid water on the snowpack’s L-band emission. However, even when pointing the radiometer along the central line of the “reflector areas”, the antenna field of view still captures radiation emanating from areas surrounding the metal-mesh reflector. Accordingly, it is necessary to separate  $T_{B,R}^p(\theta)$  from  $T_{B,R,m}^p(\theta)$  measured (m) along the azimuth direction of the reflector. The corresponding procedures, used similarly in [27,30,44], are outlined below.

Measurements (m)  $T_{B,R,m}^p(\theta)$  taken along the azimuth direction of the “reflector area” are represented as the linear combination of radiances  $T_{B,R}^p(\theta)$  and  $T_{B,N}^p(\theta)$  originating from areas covered by the reflector (R) and natural (N) areas surrounding the reflector, respectively:

$$T_{B,R,m}^p(\theta) = \mu_R^p(\theta) \cdot T_{B,R}^p(\theta) + (1 - \mu_R^p(\theta)) \cdot T_{B,N}^p(\theta) \quad (10)$$

Here we further assume that emission from areas surrounding the reflector can be represented by measurements  $T_{B,N}^p(\theta)$  performed on the “natural areas” shown in Figure 1. The factors  $\mu_R^p(\theta)$  and  $(1 - \mu_R^p(\theta))$  in Equation (10) express, respectively, the weightings of  $T_{B,R}^p(\theta)$  and  $T_{B,N}^p(\theta)$  for nadir angles  $\theta = 30^\circ, 35^\circ, \dots, 65^\circ$  and polarization  $p = H$  and  $V$ . Once  $\mu_R^p(\theta)$  is known,  $T_{B,R}^p(\theta)$  are computed from measurements  $T_{B,R,m}^p(\theta)$  and  $T_{B,N}^p(\theta)$  using Equation (10) solved for  $T_{B,R}^p(\theta)$ :

$$T_{B,R}^p(\theta) = \frac{T_{B,R,m}^p(\theta) - (1 - \mu_R^p(\theta)) \cdot T_{B,N}^p(\theta)}{\mu_R^p(\theta)} \quad (11)$$

The weighting factors  $\mu_R^p(\theta)$  in Equation (11) are derived on a daily basis using exclusively  $T_{B,R,m}^p(\theta)$  and  $T_{B,N}^p(\theta)$  measured quasi-simultaneously at night (00:00–07:00). It is essential to use exclusively night measurements for the computation of  $\mu_R^p(\theta)$ , which is representative of the corresponding day, because spatial heterogeneities across the field site are expected to be generally diminished during the night when temperature drops below freezing. This instance is in support of the assumption made that measurements  $T_{B,N}^p(\theta)$  performed over “natural areas” (Figure 1) are also representative of areas surrounding the reflector. However, this assumption is still considered critical, especially during relatively warm and transient conditions where spatial variability of, for example, ground permittivity  $\varepsilon_G$  is increased (as proven by corresponding in-situ measurements shown in Figure 4). However, throughout the main period of interest (i.e., cold winter and early spring periods), the ground is homogeneously frozen. Thus, using measurements  $T_{B,N}^p(\theta)$  to represent emission of areas surrounding the “reflector areas” is reasonable in most cases.

Another important reason to estimate  $\mu_R^p(\theta)$  from night measurements of  $T_{B,R,m}^p(\theta)$  and  $T_{B,N}^p(\theta)$  is that a surface-thawed snowpack refreezes overnight, and thus snow emission during cold nights is almost always zero [13,22,23]. As a consequence, during the cold nights throughout our main periods of interest (cold winter and early spring),  $T_{B,R}^p(\theta)$  correspond with downwelling sky brightness temperatures  $T_{sky}(\theta)$  reflected by the metal-mesh reflector towards the antenna aperture. Accordingly,  $T_{B,R}^p(\theta) = T_{sky}(\theta)$  is used in Equation (10), yielding the following expression to compute  $\mu_R^p(\theta)$  with  $T_{sky}(\theta)$  simulated by the model [32]:

$$\mu_R^p(\theta) = \frac{T_{B,N}^p(\theta) - T_{B,R,m}^p(\theta)}{T_{B,N}^p(\theta) - T_{sky}(\theta)} \quad (12)$$

In summary, the weighting factors  $\mu_R^p(\theta)$  are computed with Equation (12) for each day using the corresponding night measurements of  $T_{B,R,m}^p(\theta)$ ,  $T_{B,N}^p(\theta)$  and with  $T_{sky}(\theta)$  simulated using [32].  $\mu_R^p(\theta)$  is then kept constant throughout that day and used in Equation (11) to derive  $T_{B,R}^p(\theta)$  for that day from the corresponding quasi-synchronous measurements  $T_{B,R,m}^p(\theta)$  and  $T_{B,N}^p(\theta)$ .

## 5. Analysis of Brightness Temperatures

### 5.1. Methodology for the Analysis of L-Band Brightness Temperatures' Response to Snow Liquid Water

The model used to simulate L-band brightness temperatures  $T_B^p$  of a rough ground surface beneath a snowpack is a composite of components adopted from the L-band Microwave Emission of the Biosphere “L—MEB” model [45] and the Microwave Emission Model of Layered Snowpacks “MEMLS” [10,46] while considering simplifications applicable to L-band. The resultant L-band Specific emission model, henceforth denoted as “LS—MEMLS”, is now outlined following the model structure illustrated in Figure 9.

Block 1 of the diagram (Figure 9a) shows the “LS—MEMLS” inputs, which are the radiometer nadir angle  $\theta$ , polarization  $p = H$  (for horizontal) and  $p = V$  (for vertical), and the L-band vacuum wavelength  $\lambda = 21$  cm. Air temperature  $T_{air}$  2 m above ground, specific air humidity  $q_{air}$ , rain rate

$r_{\text{air}}$ , and the altitude  $h_{\text{site}}$  of the test site above sea-level are additional inputs necessary to simulate downwelling L-band sky radiance  $T_{\text{sky}}$  using the model described in both [32,33].

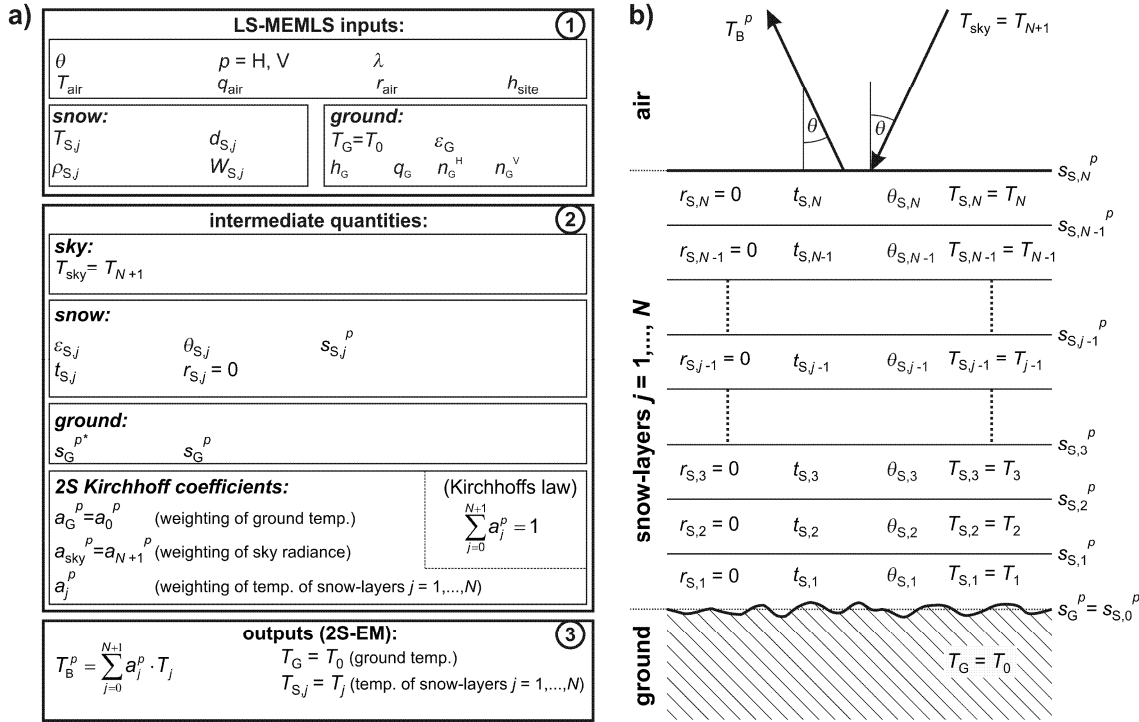


**Figure 9.** (a) Block diagram of the L-band Specific Microwave Emission Model of Layered Snowpacks (“LS—MEMLS”) used to simulate L-band brightness temperatures  $T_B^p$  over snow covered grounds; and (b) sketch of the two-stream emission model (2S-EM) employed in “LS—MEMLS”. Symbols and model components are explained in the text.

The “LS—MEMLS” inputs given to each of the layers  $j$  of the snowpack (S) are the layer-thickness  $d_{S,j}$ , the physical temperature  $T_{S,j}$ , the mass density  $\rho_{S,j}$ , and the volumetric liquid water content  $W_{S,j}$ . Inputs used to characterize the ground (G) beneath the snowpack are effective ground temperature  $T_G$ , ground permittivity  $\epsilon_G$ , and the HQN ground roughness model [45,47] parameters  $h_G$ ,  $q_G$  and  $n_G^p$  ( $p = H, V$ ) used and described in [48]. Intermediate quantities computed along with the evaluation of “LS—MEMLS” are listed in Block 2 of Figure 9a, and outlined here.

As mentioned above, L-band sky radiance  $T_{\text{sky}}$  is simulated from the “LS—MEMLS” inputs  $\theta$ ,  $T_{\text{air}}$ ,  $q_{\text{air}}$ ,  $r_{\text{air}}$ ,  $h_{\text{site}}$  based on [32]. The same approach is also used in our earlier work [14] to represent  $T_{N+1} = T_{\text{sky}}$  incident on the uppermost interface  $j = N + 1$  of the snowpack. For  $h_{\text{site}} = 1450$  m (specific to the Davos Laret site),  $T_{\text{air}} = 273.15$  K,  $q_{\text{air}} = 10$  g kg<sup>-1</sup>,  $r_{\text{air}} = 0$  mm h<sup>-1</sup>, and the considered nadir angles  $30^\circ \leq \theta \leq 65^\circ$ , sky radiance is in the range  $4.2$  K  $\leq T_{\text{sky}} \leq 5.8$  K, revealing that the atmosphere is largely transparent at L-band.

Complex snow permittivities  $\epsilon_{S,j} = \epsilon'_{S,j} + i \cdot \epsilon''_{S,j}$  are computed with the Maxwell–Garnett dielectric model considering a two-phase mixture of liquid water with permittivity  $\epsilon_W$  and dry snow with permittivity  $\epsilon_{S,\text{dry},j}$ :

$$\epsilon_{S,j} = \frac{(1-W_S) \cdot \epsilon_{S,\text{dry},j} + W_S \cdot \epsilon_W \cdot K}{1 - W_S \cdot (1-K)} \quad \text{with } K = \frac{K_a + K_b + K_c}{3} \quad \text{and} \quad (13)$$

$$K_a = \frac{\epsilon_{S,\text{dry},j}}{\epsilon_{S,\text{dry},j} + A_a (\epsilon_W - \epsilon_{S,\text{dry},j})} \quad K_b = K_c = \frac{\epsilon_{S,\text{dry},j}}{\epsilon_{S,\text{dry},j} + A_b (\epsilon_W - \epsilon_{S,\text{dry},j})}$$

The same approach is implemented in the latest version of “MEMLS” (pages 15–16 in the “MEMLS-III” manual [49]). Liquid snow water with volumetric content  $W_S$  is taken as prolate

ellipsoidal inclusions in dry snow considered as the dielectric background, and the depolarization factors are assumed as  $A_a = 0.005$ ,  $A_b = A_c = 0.4975$  [23,50].

Permittivity  $\epsilon_W = 85.82 + i \cdot 12.64$  at the frequency 1.4 GHz and at freezing temperature (273.15 K) is computed with the model [51]. Permittivity  $\epsilon_{S,dry,j}$  of the dry snow phase is computed from snow mass-density  $\rho_{S,j}$  using the same model as in “MEMLS” [ $\rho_S^* = 0.001 \cdot \rho_{S,j}$  in units of  $[g\ cm^{-3}]$ ):

$$\epsilon_{S,dry,j}(\rho_S^*) = \begin{cases} 1 + 1.5995 \cdot \rho_S^* + 1.861 \cdot \rho_S^{*3} & \text{for } 0\ g\ cm^{-3} \leq \rho_S^* \leq 0.4\ g\ cm^{-3} \\ ((1 - \nu) \cdot \epsilon_h + \nu \cdot \epsilon_b)^3 & \text{for } \rho_S^* \geq 0.4\ g\ cm^{-3} \end{cases} \quad (14)$$

with  $\nu = \rho_S^*/0.917$ ,  $\epsilon_h = 0.99913$  and  $\epsilon_b = 1.4759$ . For dry snow ( $W_S = 0.0\ m^3\ m^{-3}$ ) with mass density  $0\ kg\ m^{-3} \leq \rho_S \leq 400\ kg\ m^{-3}$ , imaginary parts  $0 \leq \epsilon_S'' \leq 1.2 \cdot 10^{-4}$  are very small and significantly smaller than real parts  $1 \leq \epsilon_S' \leq 1.759$ . This explains the very large L-band penetration depth (>300 m) in dry snow [22,23], which allows a dry snow layer to be treated as transparent (transmissivity  $t_{S,j} = 1$ ). However, for a moist snow layer,  $t_{S,j}$  rapidly decreases with increasing  $W_{S,j}$ . Accordingly, for  $W_{S,j} > 0.0\ m^3\ m^{-3}$ , transmissivity  $t_{S,j}$  is computed from the layers nadir optical-depth  $d_{S,j} \cdot \alpha_{S,j}$  and the propagation angle  $\theta_{S,j}$  across the layer  $j$  with thickness  $d_j$  and the power absorption coefficient  $\alpha_{S,j}$ . Following Beer’s and Snell’s law, this yields:

$$t_{S,j} = \exp(-d_{S,j} \cdot \alpha_{S,j} / \cos \theta_{S,j}) \quad (15)$$

and

$$\theta_{S,j} = \arcsin\left(\frac{\sin(\theta)}{\sqrt{|\epsilon_{S,j}|}}\right) \quad (16)$$

The power absorption coefficient  $\alpha_{S,j}$  within the snow-layer  $j$  is computed from the respective snow permittivity  $\epsilon_{S,j} = \epsilon'_{S,j} + i \cdot \epsilon''_{S,j}$  as:

$$\alpha_{S,j} = \frac{4\pi}{\lambda} \cdot \text{Im}\left(\sqrt{\epsilon_{S,j}}\right) \quad (17)$$

In accordance with earlier work [13,14], the volume reflectivities of snow layers are assumed to be  $r_{S,j} = 0$ , indicating the fact that volume scattering caused by snow microstructures is negligible at L-band. Clearly, neglecting snow volume scattering is applicable only in absence of prominent macrostructures (such as ice lenses) with dimensions of the order of  $\lambda$ .

Specular reflectivities  $s_{S,j}^p$  ( $p = H, V$ ) of the upper interface of each layer  $j$  result from the dielectric contrast between the respective layer permittivities  $\epsilon_{S,j}$  and  $\epsilon_{S,j+1}$ . Accordingly,  $s_{S,j}^p$  are computed with Fresnel’s equations considering  $\epsilon_{out} = \epsilon_{S,j}$  and  $\epsilon_{in} = \epsilon_{S,j+1}$  as the permittivities of the layers containing the propagated (out) and the incident (in) waves, respectively. Furthermore, the incident-angle  $\theta_{in} = \theta_{S,j+1}$  at the interface  $j = 1, \dots, N-1$  is computed using Equation (16) to correspond with the propagation angle within the above layer  $j+1$ :

$$s_{S,j}^H = \frac{\left| \frac{\sqrt{\epsilon_{in}} \cdot A - \sqrt{\epsilon_{out}} \cdot B}{\sqrt{\epsilon_{in}} \cdot A + \sqrt{\epsilon_{out}} \cdot B} \right|}{A = \cos \theta_{in}} \quad s_{S,j}^V = \frac{\left| \frac{\sqrt{\epsilon_{out}} \cdot A - \sqrt{\epsilon_{in}} \cdot B}{\sqrt{\epsilon_{out}} \cdot A + \sqrt{\epsilon_{in}} \cdot B} \right|}{B = \sqrt{1 - (1 - A^2) \epsilon_{in} / \epsilon_{out}}} \quad \text{with} \quad \epsilon_{out} = \epsilon_{S,j} \quad \epsilon_{in} = \epsilon_{S,j+1} \quad (18)$$

Likewise, the reflectivities  $s_{S,N}^H, s_{S,N}^V$  of the snow-air interface ( $j = N$ ) are computed via Equation (18) considering  $\epsilon_{in} = \epsilon_{air} = 1$ ,  $\epsilon_{out} = \epsilon_{S,j}$  and the radiometer nadir angle  $\theta_{in} = \theta$ .

In contrast to the  $j = 1, \dots, N$  specular snow-layer interface reflectivities  $s_{S,j}^p$ , the effects of ground roughness are indeed considered in the computation of the reflectivities  $s_G^p = s_{S,0}^p$  of the ground-snow interface ( $j = 0$ ). Thereto, first the specular (\*) ground-snow interface reflectivities  $s_G^{*H}$  and  $s_G^{*V}$  are computed using Equation (18) with  $\epsilon_{in} = \epsilon_{S,1}$ ,  $\epsilon_{out} = \epsilon_G$  and  $\theta_{in} = \theta_{S,1}$ . Accordingly, the dominant effect of snow refraction is incorporated into “LS—MEMLS” at this point. Next, the effect of ground

surface roughness is taken into account by correcting the specular reflectivities  $s_G^{*H}$  and  $s_G^{*V}$  using the semi-empirical HQN roughness model [45–47]

$$\begin{aligned} s_G^H &= \exp\left(-h_G \cdot (\cos \theta_{S,1})^{n_G^H}\right) \cdot (s_G^{*H} \cdot (1 - q_G) + q_G \cdot s_G^{*V}) \\ s_G^V &= \exp\left(-h_G \cdot (\cos \theta_{S,1})^{n_G^V}\right) \cdot (s_G^{*V} \cdot (1 - q_G) + q_G \cdot s_G^{*H}) \end{aligned} \quad (19)$$

Detailed information on the HQN roughness model and its typical parameter values for different types of landscapes can be found in Section 3.1.2 and Table II in [52]. However, in all of our investigations, roughness effects are assumed to be independent of the incidence angle  $\theta_{S,1}$  on the ground. For this reason, we set  $n_G^V = n_G^H = 0$ . The polarization mixing parameter is assumed to be  $q_G = 0.05$ . The most influential HQN roughness model parameter is the dimensionless effective surface roughness parameter  $h_G$ , which is mostly correlated with “geometric roughness”. The values ultimately selected for the four HQN model ground surface roughness parameters  $(h_G, q_G, n_G^V, n_G^H) = (0.1, 0.05, 0.0, 0.0)$  are in agreement with the values used in the current SMOS soil moisture retrieval algorithm [53].

As indicated in Block 3 in Figure 9a, final outputs  $T_B^p$  of “LS—MEMLS” are computed with the two-stream emission model (2S-EM) employed in “MEMLS” [10,46] using the intermediate quantities (for snow-layers  $j$ :  $t_{S,j}$ ,  $r_{S,j}$ ,  $T_{S,j}$ ; for the ground:  $s_G^p = s_{S,0}^p$ ; for the sky:  $T_{sky}$ ) made available as outlined above. The 2S-EM “balances” in each layer the up- and down-welling energy streams (fluxes) propagated by the electromagnetic waves by taking into account the boundary conditions at layer interfaces and considering Kirchhoff’s law. These (incoherent) linkages between up- and down-welling layer-fluxes take into consideration multiple reflections between the layers’ interfaces. Formulating the resulting four flux-equations for each layer (up- and down-welling at the respective two layer interfaces) yields a matrix equation for the vector  $T_B^p = (T_{B,1}^p, T_{B,2}^p, \dots, T_{B,j}^p, \dots, T_{B,N-1}^p, T_{B,N}^p, T_B^p)$  containing the upwelling radiances  $T_{B,j}^p$  across the  $j = 1, \dots, N$  snow-layers, and, as the last element  $N + 1$ , the upwelling radiance above the uppermost snow layer corresponding to the sought  $T_B^p = T_{B,N+1}^p$  above the snow covered ground. The detailed derivation of the matrix formulation of the 2S-EM can be found in Section 3 of [49].

In the alternative formulation sketched in Figure 9a,  $T_B^p$  is written as  $T_B^p = \sum_{j=0}^{N+1} a_j^p \cdot T_j$  whereas the Kirchhoff coefficients  $a_0^p = a_G^p$ ,  $a_j^p = a_{S,j}^p$  ( $j = 1, \dots, N$ ), and  $a_{j+1}^p = a_{sky}^p$  fulfill  $\sum_{j=0}^{N+1} a_j^p = 1$  and weight the respective temperatures  $T_0 = T_G$ ,  $T_j = T_{S,j}$  ( $j = 1, \dots, N$ ), and  $T_{j+1} = T_{sky}$ . This so-called Kirchhoff formulation is appropriate for small numbers  $N$  of snow layers. In the case of  $N = 1$  snow layer ( $s_{S,1}^p = s_S^p$ ,  $t_{S,1} = t_S$ ) and assuming  $r_{S,1} = r_S = 0$ , the associated 2S-EM Kirchhoff coefficients read (Appendix of [14]):

$$\begin{aligned} a_G^p &= \frac{(1-s_G^p)(1-s_S^p)t_S}{1+r_S^2 s_G^p s_S^p - r_S(s_G^p + s_S^p) - s_G^p s_S^p t_S^2} \\ a_S^p &= \frac{(1-s_G^p)(1-r_S-t_S)(1-r_S s_G^p + s_G^p t_S)}{(1-r_S s_G^p)(1-r_S s_S^p) - s_G^p s_S^p t_S^2} \\ a_{sky}^p &= 1 - a_G^p - a_S^p \end{aligned} \quad (20)$$

Brightness temperatures  $T_B^p$  above a homogeneous moist ( $t_S < 1$ ) snowpack above a given ground is therefore simulated as:

$$T_B^p = a_G^p \cdot T_G + a_S^p \cdot T_S + a_{sky}^p \cdot T_{sky} \quad (21)$$

This one-layer version of “LS—MEMLS” is employed in Figure 10a to simulate impacts of uniformly distributed snow liquid water on brightness temperatures. Furthermore, the simplicity of the one-layer version is the method of choice when “LS—MEMLS” is used in an iterative retrieval scheme. For more complex assumptions made, for instance, on the vertical distribution of snow liquid water (Figure 10b–d), the matrix formation of the 2S-EM is used.

## 5.2. Sensitivities of Brightness Temperatures to Liquid Snow Water

Following the model Equations (13) and (14), effective snow permittivities  $\epsilon_S = \epsilon'_S + i \cdot \epsilon''_S$  depend on both the snow mass-density  $\rho_S$  and its volumetric liquid water content  $W_S$ . For  $W_S = 0 \text{ m}^3\text{m}^{-3}$ , power absorption coefficients (Equation (17)) of dry snow ( $W_S = 0 \text{ m}^3\text{m}^{-3}$ ) with density  $\rho_S \leq 500 \text{ kg m}^{-3}$  are  $\alpha_S < 10^{-6} \text{ m}^{-1}$ , implying that any seasonal snowpack can be considered transparent ( $t_S \approx 1$ ) as long as it is dry. However, this changes drastically when  $W_S > 0 \text{ m}^3\text{m}^{-3}$ , mainly as a consequence of the strong increase in the imaginary part  $\epsilon''_S$  of snow permittivity with increasing  $W_S$ . For example, for wet snow with  $W_S = 0.05 \text{ m}^3\text{m}^{-3}$ , or even moist snow with  $W_S = 0.01 \text{ m}^3\text{m}^{-3}$  the respective absorption coefficients  $\alpha_S \approx 7.4545 \text{ m}^{-1}$  and  $\alpha_S \approx 1.44034 \text{ m}^{-1}$  are more than six orders of magnitude higher than for dry snow. From a practical point of view, this rapidly increasing absorption of snow with increasing  $W_S$  led, in the first attempt, to the omission of L-band-based retrievals ( $\rho_S, \epsilon_G$ ) of snow density and ground permittivity for not entirely dry snow conditions [15]. This, however, makes it even more important to explore the sensitivities of L-band  $T_B^p$ 's with respect to snow liquid water in support of (i) an in-depth understanding of the measured brightness temperatures discussed in Section 5.3; and (ii) the potential to estimate snow wetness based on L-band brightness temperatures.

Accordingly, “LS—MEMLS” is used to explore sensitivities of L-band  $T_{B,R}^p$  expected for moist snow atop a perfectly reflecting (R) ground and  $T_{B,N}^p$  expected for moist snow atop frozen natural (N) ground with respect to snow liquid water. Figure 10 shows simulated  $T_{B,R}^p(WC_S)$  (thin lines) and  $T_{B,N}^p(WC_S)$  (bold lines) for the nadir angles  $\theta = 0^\circ$  (black),  $\theta = 30^\circ$  (red), and  $\theta = 60^\circ$  (green). Snow mass-density is considered as  $\rho_S = 300 \text{ kg m}^{-3}$ ; ground- and snow temperatures are assumed as  $T_G = T_S = 273.15 \text{ K}$ . The parameter varied is the snow liquid water column  $WC_S = \int_0^{h_S} W_S(z) \cdot dz$ , defined as the volumetric liquid water content  $W_S$ , integrated over the entire snow depth  $h_S$ . Figure 10a is for “uniform”  $W_S = WC_S/h_S$  across snowpacks with  $0 \text{ mm} \leq WC_S \leq 70 \text{ mm}$  and snow-depth  $h_S = 0.5 \text{ m}$ . Further simulations are shown for the same range of  $WC_S$  contained in snowpacks with a moist snow-layer of thickness  $d_{W_S} = 0.1 \text{ m}$  either at the “top” (Figure 10b), “sandwiched” in between the dry snow (Figure 10c), or at the “bottom” of the dry snowpack (Figure 10d). These types of  $W_S$ -profiles are hereafter referred to as “uniform”, “top”, “sandwiched”, and “bottom”. Corresponding simulations are also conducted for  $\rho_S = 500 \text{ kg m}^{-3}$  yielding results fully consistent with those presented below.

For totally dry snowpacks, brightness temperatures  $T_{B,R}^p(WC_S = 0 \text{ mm})$  necessarily agree with the downwelling sky brightness temperature assumed as  $T_{\text{sky}} = 5 \text{ K}$  and specularly reflected at the ground (black open squares in Figure 10). A further characteristic common to all the  $T_{B,R}^p(WC_S)$  is the sharp increase with increasing  $WC_S$  for small values of  $WC_S$ , followed by gradually decreasing  $T_{B,R}^p(WC_S)$  for larger  $WC_S$ . The steeply increasing tail of  $T_{B,R}^p(WC_S)$  is explained by the strong increase in snow emission with increasing snow liquid water (see Equations (13)–(17)). The gradients  $dT_{B,R}^p/dWC_S$  become even larger for increasing nadir angles  $\theta$  as a result of longer propagation path-lengths across the wet snow. Furthermore, the steeply increasing tail of  $T_{B,R}^p(WC_S)$  at small  $WC_S$  is largely independent of polarization because volume emission of wet snow is assumed to be isotropic. The cause of the gradually decreasing tail of  $T_{B,R}^p(WC_S)$  seen with larger  $WC_S$ , is caused by increased interface reflectivity in the upper boundary of the wet snow-layer. The latter increases with increasing  $W_S$  as a result of likewise increasing permittivity (Equation (13)). Moreover, the gradually decreasing part of  $T_{B,R}^p(WC_S)$  depends significantly on  $\theta$  and polarization  $p$ , which is a consequence of the respective sensitivities of the Fresnel-like interface reflectivities (Equation (18)).

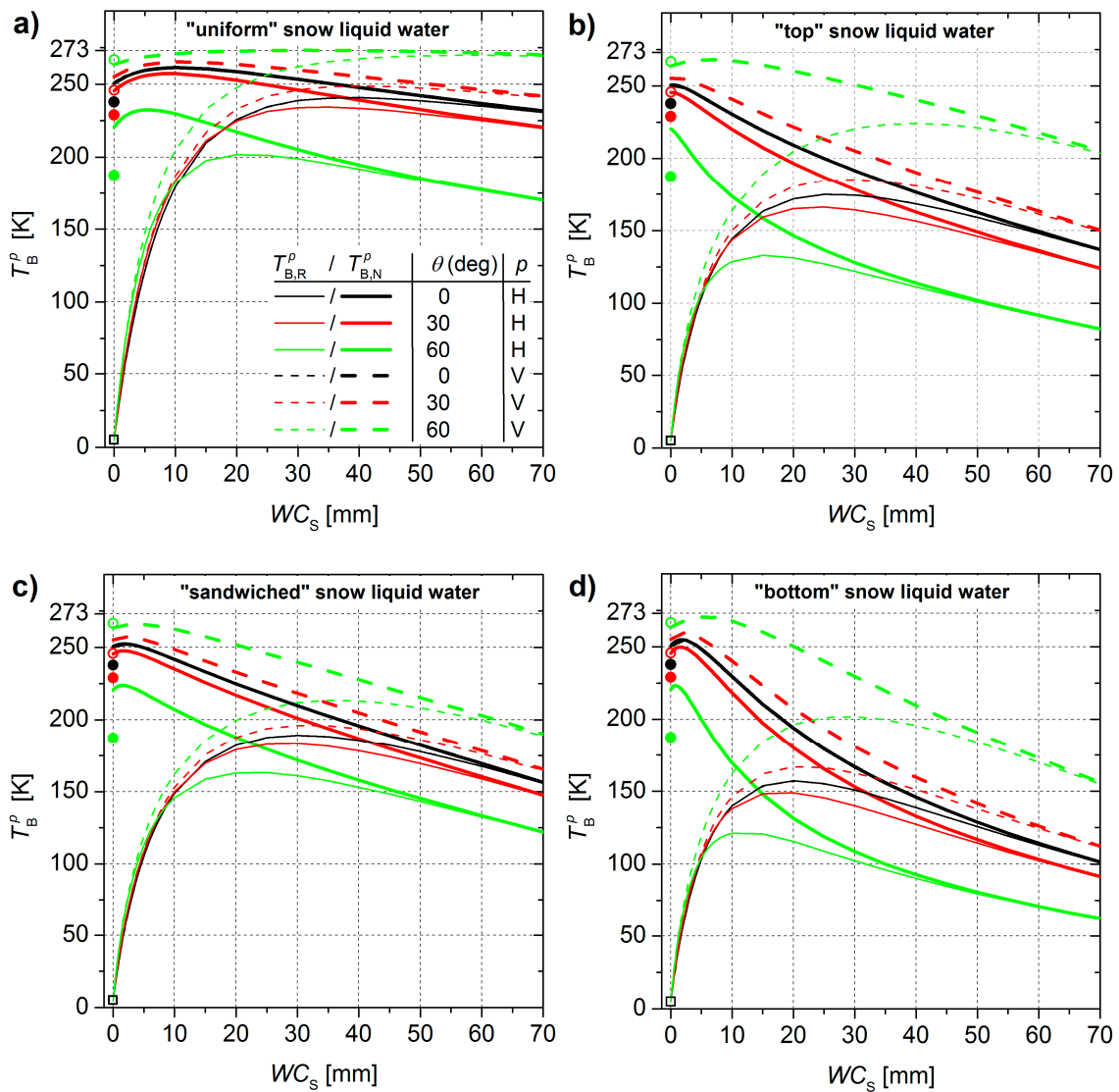


**Figure 10.** Sensitivities of brightness temperatures with respect to snow liquid water column  $WC_S$  for snow mass density  $\rho_S = 300 \text{ kg m}^{-3}$ : (a) “uniform” snow; (b) snow on “top” of the snowpack; (c) moist snow “sandwiched” in-between dry snow; and (d) a moist “bottom” snow-layer.  $T_{B,R}^p$  (thin lines) and  $T_{B,N}^p$  (bold lines) are for snow atop the reflector (R) and atop the natural (N) frozen ground with  $\varepsilon_G = 5$ , respectively. Polarization  $p = H$  (solid),  $p = V$  (dashed), and the nadir angles  $\theta = 0^\circ$  (black),  $\theta = 30^\circ$  (red), and  $\theta = 60^\circ$  (green).

The plateau of  $T_{B,R}^p(WC_S)$  occurs at intermediate values of  $WC_S$  when increasing snow volume emission compensates for decreasing interface emission. The impact of different assumptions made on the depth-profile of snow liquid water content  $W_S$  becomes apparent when comparing Figure 10a–d. For the “uniform” scenario (Figure 10a), the steeply ascending part of  $T_{B,R}^p(WC_S)$  shows larger gradients  $dT_{B,R}^p/dWC_S \gg 0 \text{ K mm}^{-1}$ , whereas the respective descending part reveals smaller sensitivities  $dT_{B,R}^p/dWC_S < 0 \text{ K mm}^{-1}$  compared to the scenarios “top” (Figure 10b), “sandwiched” (Figure 10c), and “bottom” (Figure 10d). This finding suggests that the assumption of uniformly distributed snow liquid water may lead to biased  $WC_S$ -retrievals estimated from  $T_{B,R}^p$  when liquid snow water is actually, for example, mostly present below the snow surface. Regarding the relevance of each of the considered  $W_S$ -scenarios, it should be mentioned that the corresponding scenario “sandwiched” is seen as the most realistic during the mid-winter period with pronounced diurnal

temperature variations around 0 °C. This is because strong solar short-wave radiation penetrates the first few centimeters of dry snow and can cause partial subsurface melting—a phenomenon that can be best called the “snow greenhouse effect”.

Different snow mass-densities  $\rho_S = 300 \text{ kg m}^{-3}$  (Figure 10) and  $\rho_S = 500 \text{ kg m}^{-3}$  manifest primarily in moderate offsets of  $T_{B,R}^p(WC_S)$ , while gradients  $dT_{B,R}^p/dWC_S$  are not affected greatly. The predominant and very high sensitivities of  $T_{B,R}^p$  with respect to  $WC_S$  imply the potential to retrieve snow liquid water column  $WC_S$  from measurements  $T_{B,R}^p$  performed over the “reflector areas” with high sensitivity, especially for the lower range  $0 \text{ mm} \leq WC_S \leq 20 \text{ mm}$ .

Regarding the simulations  $T_{B,N}^p(WC_S)$  (bold lines in Figure 10), representing the emission of snow atop a ground with  $\epsilon_G = 5$ , the same four  $W_S$ -scenarios “uniform” (Figure 10a), “top” (Figure 10b), “sandwiched” (Figure 10c), and “bottom” (Figure 10d) are considered. Polarization is indicated as  $p = H$  (solid),  $V$  (dashed); nadir angles  $\theta = 0^\circ$  (black),  $\theta = 30^\circ$  (red), and  $\theta = 60^\circ$  (green), all with the considered snow density  $\rho_S = 300 \text{ kg m}^{-3}$  (Figure 10).

For the completely dry snowpack ( $WC_S = 0 \text{ mm}$ ) and  $\theta = 0^\circ$  (black lines), the respective  $T_{B,N}^p(WC_S = 0 \text{ mm})$  are slightly larger than the brightness temperatures above the snow-free ground (black solid circles) because of the impedance matching of the snow as explained in [13]. For  $\theta > 0^\circ$  and  $WC_S = 0 \text{ mm}$ , the  $T_{B,N}^p(WC_S = 0 \text{ mm})$  deviate from corresponding bare-ground brightness temperatures (red circles for  $\theta = 30^\circ$ , green circles for  $\theta = 60^\circ$  and solid for  $p = H$ , open for  $p = V$ ). This deviation results from not only impedance matching, but also refraction effects caused by snow interfaces [13,14]. Most of the  $T_{B,N}^p(WC_S)$  show an increasing and a decreasing tail separated by a plateau. Again, the increasing tails of  $T_{B,N}^p(WC_S)$  result from the increasing emission of the snow-volume with increasing snow liquid water. However, they are distinctly less pronounced than the corresponding increasing tails simulated for the  $T_{B,R}^p(WC_S)$ .

This is the compelling consequence of the much larger emission of the frozen natural ground (with  $\epsilon_G = 5$ ) compared to the zero-emission of the ground covered with the reflector. The decreasing tails of  $T_{B,N}^p(WC_S)$ , caused by increased interface reflectivities, are more pronounced than the decreasing tails of  $T_{B,R}^p(WC_S)$ . This is because snow-ground interface reflectivities are much more comparable with snow-sir interface reflectivities in the case of “natural” ( $\epsilon_G = 5$ ) than in the case of the ground covered with the reflector. Accordingly,  $T_{B,N}^p$  is diminished by both increased reflectivities at the snow-sir and ground-snow interfaces, while  $T_{B,R}^p$  is exclusively diminished by increased reflectivities at the snow-sir interface. Of course, snow-ground interface reflectivities are only affecting brightness temperatures as long as the snowpack is not totally opaque. Accordingly, when brightness temperatures become dominated by snow volume emission for large  $WC_S$ , the  $T_{B,N}^p(WC_S)$  and  $T_{B,R}^p(WC_S)$  necessarily approach each other. In summary, the discussed sensitivities of  $T_{B,N}^p$  with respect to  $WC_S$  seem to be sufficiently high to achieve at least reliable qualitative information on snow wetness states based on L-band brightness temperatures measured over natural frozen grounds.

### 5.3. Analysis of Measured Brightness Temperatures

We now present the time series of measured calibrated brightness temperatures  $T_{B,R}^p(\theta)$  and  $T_{B,N}^p(\theta)$ , and discuss examples of their prominent signatures in response to selected snow and ground conditions. Figure 11a shows the time series of  $T_{B,N}^H$  and  $T_{B,R}^H$  averaged over nadir angles  $40^\circ \leq \theta \leq 50^\circ$  with blue and magenta lines, respectively. Averaging over  $\theta$  is performed to achieve more measured brightness temperatures after RFI filtering. The onset of snow cover on 3 January and the beginning of “early spring” on 31 January are indicated by vertical dashed lines. Thus, as labeled above Figure 11, the entire time series is broken into three periods: the “snow-free period”, the “cold winter period” with frozen ground and mostly  $T_{\text{air}} < 0^\circ \text{ C}$ , and the “early spring period” with air temperatures rising above the freezing point. Figure 11b shows  $T_{B,R}^V(\theta)$  and  $T_{B,N}^V(\theta)$ . Figure 11c shows air temperature  $T_{\text{air}}$  and precipitation rate, respectively.

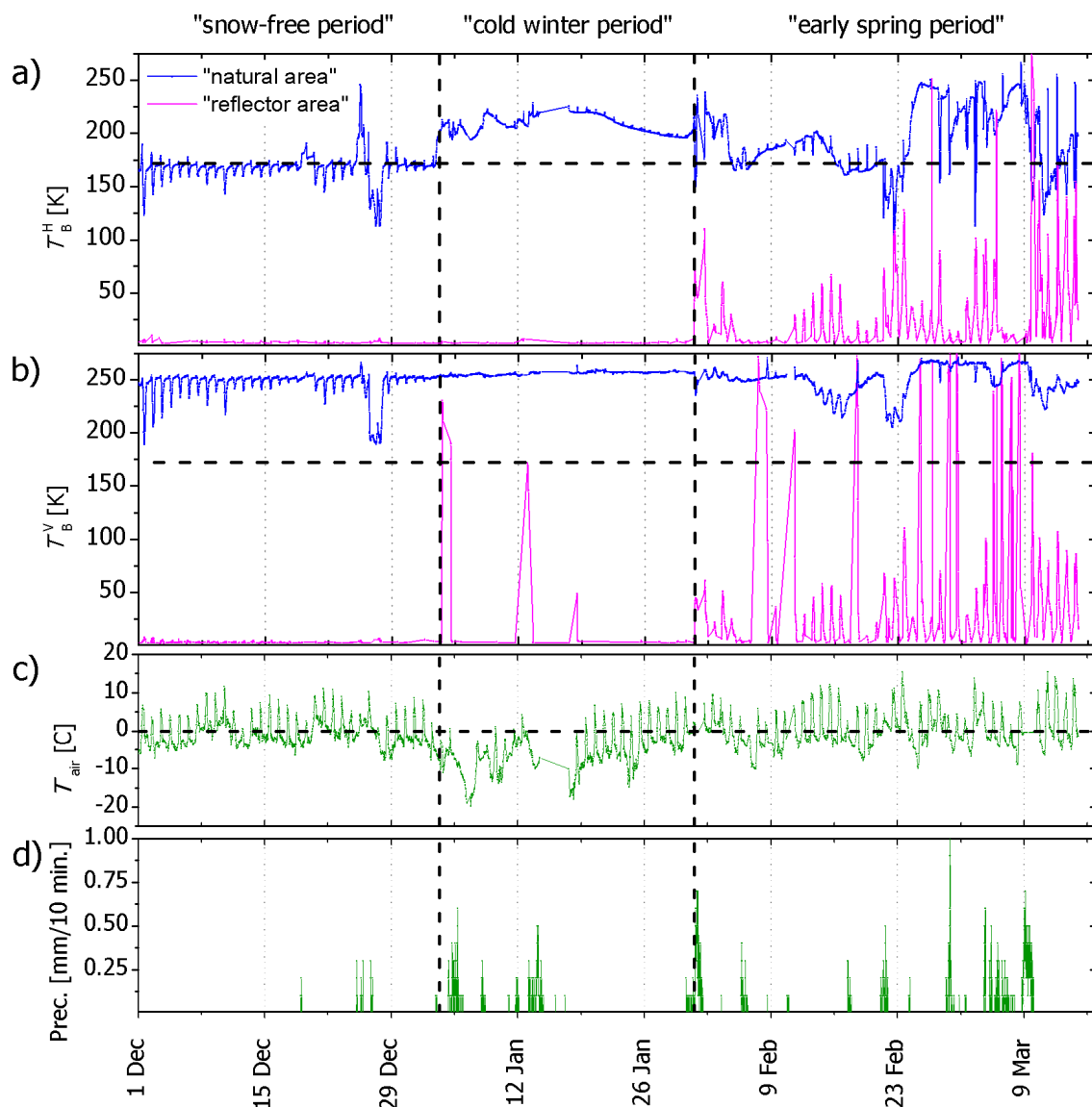


**Figure 11.**  $T_{B,N}^p$  (blue) and  $T_{B,R}^p$  (magenta) of brightness temperatures at: (a) horizontal ( $p = H$ ); and (b) vertical ( $p = V$ ) polarization measured over “natural” and “reflector” areas, respectively. Panels (c,d) show air temperature  $T_{air}$  and precipitation rate, respectively. The vertical dashed lines delimit the “snow-free period” (before 3 January), the “cold winter period” (3–31 January), and the “early spring period” (after 31 January).

As explained in Section 5.2 and shown with black open squares in Figure 10,  $T_{B,R}^p(\theta)$  ( $p = H, V$ ) simulated for the “reflector areas” equals downwelling sky radiance  $T_{sky} = T_{B,R}^p$  if the reflector is snow-free and also if the reflector is covered with entirely dry snow. These model findings are corroborated by the measurements shown in Figure 11. Throughout the snowless period,  $T_{B,R}^H$  (Figure 11a) is close to 4.5 K, which is virtually equal to  $T_{sky} \approx 4.7$  K for  $40^\circ \leq \theta \leq 50^\circ$  [32]. This holds true also after the onset of the snow cover throughout the “cold winter period” in January when the snowpack is dry. However, with the beginning of the “early spring period”,  $T_{B,R}^H$  occasionally rises distinctly above  $T_{sky}$ , which is interpreted as intermittent occurrences of snow liquid water. This is, again, consistent with the corresponding response of simulated  $T_{B,R}^H$  shown in Figure 10. On the other hand, the perception of intermittent increases in measured  $T_{B,R}^H$  caused by snow liquid water is also meaningful from the environmental conditions viewpoint because time-integrated heat-input to the snowpack starts temporarily rising above the ice latent-heat during the “early spring period”.

The distinct sensitivity of  $T_{B,R}^H$  with respect to snow liquid water becomes even more evident during the period 9–23 February, when  $T_{B,R}^H$  reaches its maximum every day in the afternoon and falls to  $T_{sky}$  over night when the snowpack refreezes. Accordingly, the measured temporal characteristics of  $T_{B,R}^H$  clearly indicate the onset of “early-spring snow”.

Additionally, during the aforementioned two weeks in February, where the  $T_{B,R}^H$  shows exclusively sharp increases during the afternoon hours, the concurrent  $T_{B,N}^H$  measured over the “natural areas” show both sharply increasing (11–13 February) and decreasing (16–19 February) deflections. Although at first glance these opposite measurement responses of  $T_{B,R}^H$  and  $T_{B,N}^H$  to snow wetness may seem counter-intuitive, it is in qualitative agreement with the corresponding simulations shown in Figure 10. On the one hand, the simulated  $T_{B,R}^H(WC_S)$  and  $T_{B,N}^H(WC_S)$  in Figure 10, reveal sharply increasing  $T_{B,R}^H(WC_S)$  for  $0 \text{ mm} \leq WC_S \leq 20 \text{ mm}$  explained by increased snow emission. On the other hand,  $T_{B,R}^H(WC_S)$  is expected to decrease for  $WC_S \gtrsim 20 \text{ mm}$ , while simulated  $T_{B,N}^H(WC_S)$  already decrease for lower  $WC_S \gtrsim 5 \text{ mm}$ . In other words, for  $0 \text{ mm} \leq WC_S \leq 20 \text{ mm}$ , the  $T_{B,R}^H(WC_S)$  are expected to increase steadily, while  $T_{B,N}^H(WC_S)$  increase with very little snow liquid-water ( $0 \text{ mm} \leq WC_S \leq 5 \text{ mm}$ ) and decrease with larger values  $WC_S \gtrsim 5 \text{ mm}$ . These simulation-based findings explain why measurements  $T_{B,R}^H$  and  $T_{B,N}^H$  can indeed respond in contrast to each other with respect to low  $WC_S$  values, as is expected from 9 to 23 February. The fact that “LS—MEMLS” is an incoherent emission model also implies that it is not necessary to adduct coherent effects to explain the observed oppositional responses of  $T_{B,R}^H$  and  $T_{B,N}^H$  to snow liquid water.

As mentioned earlier, Figure 11b shows similar information to Figure 11a only with “reflector areas” and “natural areas” brightness temperatures  $T_{B,R}^V$  (magenta) and  $T_{B,N}^V$  (blue) at vertical polarization. The signature in  $T_{B,R}^V$  (Figure 11b) associated with the first appearance of snow liquid water (“early-spring snow”) coincides with the corresponding response of  $T_{B,R}^H$  (Figure 11a). However, three additional distinct peaks in  $T_{B,R}^V$  are observed during measurements on 3, 13, and 18 of January. For certain, these peaks are not caused by snow liquid water because  $T_{air}$  (Figure 11c) was well below the freezing point during the “cold winter period”. The still very shallow and homogeneous snow-depth present during this period suggests that these peaks are caused by coherent effects. This supposition is further borne out by the fact that the amplitudes of the three peaks decrease with time and, consequently, with growing snow depth (see Figure 2a). Likewise, the excessively high  $T_{B,R}^V$  measured for 9 h during 7 and 8 of February are likely the result of coherent effects. In the case of the respective measurements during the beginning of the “early spring period” the suspected coherent effect is most likely induced by coherent layers of moist snow rather than by shallow snow height  $h_S$ . This is because  $h_S > 0.5 \text{ m}$  (see Figure 2a) during the “early spring period” is significantly larger than the maximum thickness  $3\lambda/8\sqrt{\epsilon_S} \cong 0.07 \text{ m}$  of a snow layer expected to induce coherent effects (see [10,49]) at L-band ( $\lambda \cong 0.21 \text{ m}$ ), while a coherent moist snow layer can develop and vanish as a result of refreezing during a day of this period.

Figure 11d shows frequent precipitation at the end of February and early March. Most of these precipitation events are rain or wet snowfall, which naturally increase snow liquid-water distinctly. Thus, the higher  $T_{B,R}^H$  and  $T_{B,R}^V$  observed over the “reflector areas” for this period are consistent with simulated responses shown in Figure 10. One should note that increased  $T_{B,R}^p$  ( $p = H, V$ ) is almost exclusively a result of increased snow wetness. Thus, neither precipitation events alone nor  $T_{air} \geq 0 \text{ }^\circ\text{C}$  imply increased  $T_{B,R}^p$  because dry snowfall does not cause more liquid snow water and snow melt-down does not occur for  $T_{air} \geq 0 \text{ }^\circ\text{C}$  unless the snowpack has reached ice latent heat.

As outlined in Section 5.1, snow liquid-water distinctly increases snow absorption. This impact is so large that the L-band penetration depth of  $>300 \text{ m}$  in dry snow drops to less than 3 m for moist snow with liquid water content of  $\sim 1\%$  and to even less than 0.3 m for wet snow with liquid water content of  $\sim 3\%$  [22,23]. Accordingly, a natural snowpack can eventually become largely opaque especially during late winter periods, implying that  $T_{B,R}^p$  are no longer dominated by the very low emissivity of the metal reflector. Accordingly, we define the snowpack as “opaque” if more than 63% of the total emission originates from the snowpack, whereas up to this limit the

snowpack is considered “semi-transparent”. Considering that the effective snow temperature for moist snow is necessarily close to the freezing-point of water, 273.15 K, the upper limit of  $T_{B,R}^p$  indicating an “opaque” snowpack is  $273.15 \times e^{-1} \approx 172$  K. The horizontal dashed lines in Figure 11a,b indicate this threshold. It can be seen that the great majority of  $T_{B,R}^p$  ( $p = H, V$ ) measurements are below this threshold, and as a result snow is still classified as “semi-transparent” rather than “opaque”. This experimental result validates the theoretically predicted advantage of L-band radiometry over higher frequency bands because of moist snow semi-transparency which is an absolute precondition to estimating snowpack column properties (such as snow liquid water-column) from remote sensing data.

Finally, we briefly interpret the  $T_{B,N}^p$  ( $p = H, V$ ) measurements during the “snow-free period” before 3 January. It can be seen in Figure 11a,b that  $T_{B,N}^p$  in both polarizations  $p = H$  and  $V$  demonstrate an evanescent fluctuation pattern synchronous and anti-correlated with the diurnal variations of  $T_{air}$ . This anti-correlation implies that the  $T_{B,N}^p$  fluctuations are not a direct result of  $T_{air}$  diurnal variations but are rather a dielectric effect. To understand these fluctuations, one should note that in the absence of a snow cover acting as a heat-insulator, daily partial thaw-up takes place at a thin surface layer of bare ground which results in slightly higher  $\epsilon_G$  and lower emissivity. This change in emissivity results in lower and higher  $T_{B,N}^p$  during days and nights, respectively. The amplitude of these fluctuations decreases with deeper freezing of soil resulting from decreasing average air temperature, shorter days, and so on. The exception to this trend takes place on 26 and 27 December when a rain precipitation event moisturizes the soil surface resulting in significantly lower  $T_{B,N}^p$  for both  $p = H$  and  $V$ , but after 27 December, the soil refreezes and  $T_{B,N}^p$  returns to the approximately same values as before the rain event.

## 6. Summary and Conclusions

The present work is to be seen as the scientific basis for upcoming research on L-band remote sensing applied to the retrieval of ground freeze/thaw state and snow volume properties, such as mass density and liquid water content. Accordingly, details regarding the Davos Laret field laboratory and its instrumentation during its first winter of operation (2016/2017) are here explained. The in-situ measurements of ground and snow state parameters, climatological data, as well as L-band brightness temperatures recorded during the first winter 2016/2017 campaign, were presented and discussed. These data provide insight into how ground-snow system evolution is influenced by the climatological drivers. The temporal evolution of the measured data suggests a three-phase partitioning of the entire campaign into “snow-free period”, “cold winter period”, and “early spring period”.

As part of ELBARA-II’s raw data processing to achieve calibrated brightness temperatures, a refined RFI mitigation approach is suggested based on fitting a Gaussian model to the distribution of measured raw-data voltage samples. Its better performance compared to conventional “normality” tests (kurtosis, skewness) is demonstrated, and its ability to quantify non-thermal disturbances  $\Delta T_B^{p,ch}$  in individual measurements is highlighted. It is considered prudent to employ  $\Delta T_B^{p,ch}$  in future retrieval schemes using data measured with radiometers that output raw data in time-domain, such as ELBARA-II and the SMAP radiometer [54]. A further improvement in the calibration of ELBARA-II brightness temperatures concerns the use of values  $L_{TL}^p$  of “effective” transmission losses, which optimally represent the extent of associated thermal noise. Accordingly, the introduced refinement minimizes under- and over-estimation of thermal noise caused by the lossy transmission line at different physical temperatures and ultimately imposed on the calibrated brightness temperatures.

The response of the brightness temperatures  $T_{B,R}^p$  and  $T_{B,N}^p$ , over “reflector areas” and “natural areas”, with respect to snow liquid water column  $WC_S$  is analyzed and presented. These analysis results reveal the high sensitivity of  $T_{B,R}^p$  and moderate, but measureable, sensitivity of  $T_{B,N}^p$  with respect to the liquid water column  $WC_S$ . These model findings were corroborated by corresponding measured time series of  $T_{B,R}^p$  and  $T_{B,N}^p$ . For example, the measured  $T_{B,R}^p$  equals the sky brightness

temperature  $T_{\text{sky}} \approx 4.7$  K for the “snow-free period” and the “cold winter cold” when the snowpack is dry. This is predicted by the corresponding simulations of  $T_{\text{B,R}}^p$  for dry snow. It was also shown that distinct daily increases in measured  $T_{\text{B,R}}^p$  indicate the onset of the snow melting season, otherwise called “early-spring snow”. The consistency between modeled and measured responses of  $T_{\text{B,R}}^p$  and  $T_{\text{B,N}}^p$  suggests the need to explore interfering effects of snow liquid water on estimates ( $\rho_s, \epsilon_G$ ) of snow density and ground permittivity retrieved with the approach [14], which inherently assumes snow to be dry. Even more noticeably, our analysis hints at the possibility of estimating snow liquid water column  $WC_S$  using L-band radiometry.

**Acknowledgments:** This paper was supported in part by the Swiss National Science Foundation under Grant 200021L\_156111 /1, and in part by ESA within the framework of ESA’s SMOS “Expert Support Laboratory” (ESL) for Level 2. Furthermore, we acknowledge the Helmholtz Centre Potsdam (GFZ) for providing the ELBARA-II radiometer funded via the German Helmholtz Associations TERrestrial ENvironmental Observatories (TERENO) infrastructure project, and Matthias Jaggi from the WSL Institute for Snow and Avalanche Research SLF for conducting in-situ snow characterization measurements. We thank Curtis Gautschi for editing the manuscript as well as Manfred Stähli for his helpful comments. In addition, the authors would like to hereby express their appreciation to the anonymous reviewers for their valuable comments and inputs which helped with further improvement of this work.

**Author Contributions:** Reza Naderpour and Mike Schwank conceived, designed, and performed the experiments in equal shares. Likewise, they contributed equally to the data analyses and the writing of the manuscript. Christian Mätzler provided valuable scientific inputs to the research presented.

**Conflicts of Interest:** The authors declare no conflict of interest.

## References

1. Mätzler, C. Cost action 712: Microwave radiometry. In *Remote Sensing of Atmosphere and Ocean from Space: Models, Instruments and Techniques*; Springer: Berlin, Germany, 2002; pp. 231–246.
2. Jackson, T.J.; Schmugge, T.J. Passive microwave remote sensing system for soil moisture: Some supporting research. *IEEE Trans. Geosci. Remote Sens.* **1989**, *27*, 225–235. [[CrossRef](#)]
3. Rautiainen, K.; Lemmetyinen, J.; Pulliainen, J.; Vehviläinen, J.; Drusch, M.; Kontu, A.; Kainulainen, J.; Seppänen, J. L-Band Radiometer Observations of Soil Processes in Boreal and Subarctic Environments. *IEEE Trans. Geosci. Remote Sens.* **2012**, *50*, 1483–1497. [[CrossRef](#)]
4. Rautiainen, K.; Lemmetyinen, J.; Schwank, M.; Kontu, A.; Ménard, C.B.; Mätzler, C.; Drusch, M.; Wiesmann, A.; Ikonen, J.; Pulliainen, J. Detection of soil freezing from L-band passive microwave observations. *Remote Sens. Environ.* **2014**, *147*, 206–218. [[CrossRef](#)]
5. Macelloni, G.; Brogioni, M.; Pampaloni, P.; Cagnati, A.; Drinkwater, M.R. DOMEX 2004: An experimental campaign at Dome-C Antarctica for the calibration of spaceborne low-frequency microwave radiometers. *IEEE Trans. Geosci. Remote Sens.* **2006**, *44*, 2642–2653. [[CrossRef](#)]
6. Roy, A.; Toose, P.; Williamson, M.; Rowlandson, T.; Derksen, C.; Royer, A.; Berg, A.A.; Lemmetyinen, J.; Arnold, L. Response of L-Band brightness temperatures to freeze/thaw and snow dynamics in a prairie environment from ground-based radiometer measurements. *Remote Sens. Environ.* **2017**, *191*, 67–80. [[CrossRef](#)]
7. Zheng, D.; Wang, X.; van der Velde, R.; Zeng, Y.; Wen, J.; Wang, Z.; Schwank, M.; Ferrazzoli, P.; Su, Z. L-Band Microwave Emission of Soil Freeze-Thaw Process in the Third Pole Environment. *IEEE Trans. Geosci. Remote Sens.* **2017**, *55*, 5324–5338. [[CrossRef](#)]
8. Mätzler, C.; Hüppi, R. Review of Signature Studies for Microwave Remote Sensing of Snowpacks. *Adv. Space Res.* **1989**, *9*, 253–265. [[CrossRef](#)]
9. Mätzler, C. Improved Born Approximation for scattering of radiation in a granular medium. *J. Appl. Phys.* **1998**, *83*, 6111–6117. [[CrossRef](#)]
10. Wiesmann, A.; Mätzler, C. Microwave emission model of layered snowpacks. *Remote Sens. Environ.* **1999**, *70*, 307–316. [[CrossRef](#)]
11. Liang, D.; Xu, X.; Tsang, L.; Andreadis, K.M.; Josberger, E.G. The Effects of Layers in Dry Snow on Its Passive Microwave Emissions Using Dense Media Radiative Transfer Theory Based on the Quasicrystalline Approximation (QCA/DMRT). *IEEE Trans. Geosci. Remote Sens.* **2008**, *46*, 3663–3671. [[CrossRef](#)]

12. Harlow, R.C.; Essery, R. Tundra Snow Emissivities at MHS Frequencies: MEMLS Validation Using Airborne Microwave Data Measured During CLPX-II. *IEEE Trans. Geosci. Remote Sens.* **2012**, *50*, 4262–4278. [[CrossRef](#)]
13. Schwank, M.; Rautiainen, K.; Mätzler, C.; Stähli, M.; Lemmetyinen, J.; Pulliainen, J.; Vehviläinen, J.; Kontu, A.; Ikonen, J.; Ménard, C.B.; et al. Model for microwave emission of a snow-covered ground with focus on L band. *Remote Sens. Environ.* **2014**, *154*, 180–191. [[CrossRef](#)]
14. Schwank, M.; Mätzler, C.; Wiesmann, A.; Wegmüller, U.; Pulliainen, J.; Lemmetyinen, J.; Rautiainen, K.; Derksen, C.; Toose, P.; Drusch, M. Snow Density and Ground Permittivity Retrieved from L-Band Radiometry: A Synthetic Analysis. *IEEE J. Sel. Top. Appl. Earth Obs. Remote Sens.* **2015**, *8*, 3833–3845. [[CrossRef](#)]
15. Lemmetyinen, J.; Schwank, M.; Rautiainen, K.; Kontu, A.; Parkkinen, T.; Mätzler, C.; Wiesmann, A.; Wegmüller, U.; Derksen, C.; Toose, P.; et al. Snow density and ground permittivity retrieved from L-band radiometry: Application to experimental data. *Remote Sens. Environ.* **2016**, *180*, 377–391. [[CrossRef](#)]
16. Naderpour, R.; Schwank, M.; Mätzler, C.; Lemmetyinen, J.; Steffen, K. Snow Density and Ground Permittivity Retrieved From L-Band Radiometry: A Retrieval Sensitivity Analysis. *IEEE J. Sel. Top. Appl. Earth Obs. Remote Sens.* **2017**, *10*, 3148–3161. [[CrossRef](#)]
17. Schwank, M.; Wiesmann, A.; Werner, C.; Mätzler, C.; Weber, D.; Murk, A.; Völksch, I.; Wegmüller, U. ELBARA II, An L-Band Radiometer System for Soil Moisture Research. *Sensors* **2010**, *10*, 584–612. [[CrossRef](#)] [[PubMed](#)]
18. Kerr, Y.H.; Waldteufel, P.; Wigneron, J.P.; Delwart, S.; Cabot, F.; Boutin, J.; Escorihuela, M.J.; Font, J.; Reul, N.; Gruhier, C.; et al. The SMOS mission: New tool for monitoring key elements of the global water cycle. *Proc. IEEE* **2010**, *98*, 666–687. [[CrossRef](#)]
19. De Jeu, R.; Holmes, T.R.H.; Owe, M. Deriving land surface parameters from 3 different vegetated sites with the ELBARA 1.4 GHz passive microwave radiometer. In Proceedings of the Remote Sensing of Agriculture, Ecosystems, and Hydrology V (SPIE), Barcelona, Spain, 8–12 September 2003; Volume 5232.
20. Saleh, K.; Wigneron, J.-P.; Waldteufel, P.; de Rosnay, P.; Schwank, M.; Calvet, J.-C.; Kerr, Y.H. Estimates of Surface Soil Moisture under Grass Covers using L-band Radiometry. *Remote Sens. Environ.* **2007**, *109*, 42–53. [[CrossRef](#)]
21. Wigneron, J.P.; Chanzy, A.; Kerr, Y.H.; Lawrence, H.; Shi, J.; Escorihuela, M.J.; Mironov, V.; Mialon, A.; Demontoux, F.; de Rosnay, P.; et al. Evaluating an Improved Parameterization of the Soil Emission in L-MEB. *IEEE Trans. Geosci. Remote Sens.* **2011**, *49*, 1177–1189. [[CrossRef](#)]
22. Hofer, R.; Mätzler, C. Investigations on snow parameters by radiometry in the 3- to 60-mm wavelength region. *J. Geophys. Res.* **1980**, *85*, 453. [[CrossRef](#)]
23. Mätzler, C.; Aebischer, H.; Schanda, E. Microwave dielectric properties of surface snow. *IEEE J. Ocean. Eng.* **1984**, *9*, 366–371. [[CrossRef](#)]
24. Pulliainen, J.; Hallikainen, M. Retrieval of Regional Snow Water Equivalent from Space-Borne Passive Microwave Observations. *Remote Sens. Environ.* **2001**, *75*, 76–85. [[CrossRef](#)]
25. Kaleschke, L.; Tian-Kunze, X.; Maaß, N.; Mäkynen, M.; Drusch, M. Sea ice thickness retrieval from SMOS brightness temperatures during the Arctic freeze-up period. *Geophys. Res. Lett.* **2012**, *39*. [[CrossRef](#)]
26. Bogaen, H.R.; Huisman, J.A.; Schilling, B.; Weuthen, A.; Vereecken, H. Effective calibration of low-cost soil water content sensors. *Sensors* **2017**, *17*, 208. [[CrossRef](#)] [[PubMed](#)]
27. Schwank, M.; Wigneron, J.P.; Lopez-Baeza, E.; Völksch, I.; Mätzler, C.; Kerr, Y. L-Band Radiative Properties of Vine Vegetation at the SMOS Cal/Val Site MELBEX III. *IEEE Trans. Geosci. Remote Sens.* **2012**, *50*, 1587–1601. [[CrossRef](#)]
28. Mätzler, C.; Weber, D.; Wüthrich, M.; Schneeberger, K.; Stamm, C.; Wydler, H.; Fluhler, H. ELBARA, the ETH L-band radiometer for soil-moisture research. In Proceedings of the 2003 IEEE International Geoscience and Remote Sensing Symposium (IEEE Cat. No.03CH37477), Toulouse, France, 21–25 July 2003; Volume 5, pp. 3058–3060.
29. Institute of Applied Physics. *Handbook of the MORA 11.4 GHz Radiometer*; Institute of Applied Physics: Bern, Switzerland, 1991.
30. Guglielmetti, M.; Schwank, M.; Mätzler, C.; Oberdörster, C.; Vanderborght, J.; Flühler, H. FOSMEX: Forest Soil Moisture Experiments with Microwave Radiometry. *IEEE Trans. Geosci. Remote Sens.* **2008**, *46*, 727–735. [[CrossRef](#)]

31. Werner, C.; Wiesmann, A.; Strozzi, T.; Schneebeli, M.; Matzler, C. The snowscat ground-based polarimetric scatterometer: Calibration and initial measurements from Davos Switzerland. In Proceedings of the 2010 IEEE International Geoscience and Remote Sensing Symposium, Honolulu, HI, USA, 25–30 July 2010; pp. 2363–2366.
32. Pellarin, T.; Wigneron, J.-P.; Calvet, J.-C.; Berger, M.; Douville, H.; Ferrazzoli, P.; Kerr, Y.H.; Lopez-Baeza, E.; Pulliainen, J.; Simmonds, L.P. Two-year global simulation of L-band brightness temperatures over land. *IEEE Trans. Geosci. Remote Sens.* **2003**, *41*, 2135–2139. [[CrossRef](#)]
33. Loth, B.; Graf, H.-F.; Oberhuber, J.M. Snow cover model for global climate simulations. *J. Geophys. Res.* **1993**, *98*, 10451–10464. [[CrossRef](#)]
34. Tarongi, J.M.; Camps, A. Normality Analysis for RFI Detection in Microwave Radiometry. *Remote Sens.* **2010**, *2*, 191–210. [[CrossRef](#)]
35. Le Vine, D.M. ESTAR experience with RFI at L-band and implications for future passive microwave remote sensing from space. In Proceedings of the IEEE International Geoscience and Remote Sensing Symposium, Toronto, ON, Canada, 24–28 June 2002; pp. 847–849.
36. Li, L.; Njoku, E.G.; Im, E.; Chang, P.S.; Germain, K.S. A preliminary survey of radio-frequency interference over the US in Aqua AMSR-E data. *IEEE Trans. Geosci. Remote Sens.* **2004**, *42*, 380–390. [[CrossRef](#)]
37. Njoku, E.G.; Ashcroft, P.; Chan, T.K.; Li, L. Global survey and statistics of radio-frequency interference in AMSR-E land observations. *IEEE Trans. Geosci. Remote Sens.* **2005**, *43*, 938–947. [[CrossRef](#)]
38. Massey, F.J., Jr. The Kolmogorov-Smirnov test for goodness of fit. *J. Am. Stat. Assoc.* **1951**, *46*, 68–78. [[CrossRef](#)]
39. Lilliefors, H.W. On the Kolmogorov-Smirnov test for normality with mean and variance unknown. *J. Am. Stat. Assoc.* **1967**, *62*, 399–402. [[CrossRef](#)]
40. Ruf, C.S.; Gross, S.M.; Misra, S. RFI detection and mitigation for microwave radiometry with an agile digital detector. *IEEE Trans. Geosci. Remote Sens.* **2006**, *44*, 694–706. [[CrossRef](#)]
41. Roo, R.D.D.; Misra, S.; Ruf, C.S. Sensitivity of the Kurtosis Statistic as a Detector of Pulsed Sinusoidal RFI. *IEEE Trans. Geosci. Remote Sens.* **2007**, *45*, 1938–1946. [[CrossRef](#)]
42. Misra, S.; Ruf, C.S. Detection of Radio-Frequency Interference for the Aquarius Radiometer. *IEEE Trans. Geosci. Remote Sens.* **2008**, *46*, 3123–3128. [[CrossRef](#)]
43. Johnson, J.T.; Potter, L.C. Performance Study of Algorithms for Detecting Pulsed Sinusoidal Interference in Microwave Radiometry. *IEEE Trans. Geosci. Remote Sens.* **2009**, *47*, 628–636. [[CrossRef](#)]
44. Schwank, M.; Guglielmetti, M.; Mätzler, C.; Flüßler, H. Testing a New Model for the L-band Radiation of Moist Leaf Litter. *IEEE Trans. Geosci. Remote Sens.* **2008**, *46*, 1982–1994. [[CrossRef](#)]
45. Wigneron, J.-P.; Kerr, Y.; Waldteufel, P.; Saleh, K.; Richaume, P.; Ferrazzoli, P.; Escorihuela, M.-J.; Grant, J.P.; Hornbuckle, B.; de Rosnay, P.; et al. L-band microwave emission of the biosphere (L-MEB) model: Description and calibration against experimental data sets over crop fields. *Remote Sens. Environ.* **2007**, *107*, 639–655. [[CrossRef](#)]
46. Mätzler, C.; Wiesmann, A. Extension of the microwave emission model of layered snowpacks to coarse-grained snow. *Remote Sens. Environ.* **1998**, *70*, 317–325. [[CrossRef](#)]
47. Wigneron, J.-P.; Laguerre, L.; Kerr, Y.H. A simple parameterization of the L-band microwave emission from rough agricultural soils. *IEEE Trans. Geosci. Remote Sens.* **2001**, *39*, 1697–1707. [[CrossRef](#)]
48. Flores, A.N.; Entekhabi, D.; Bras, R.L.; Ivanov, V.Y. Hillslope-Scale Controls on Remote Sensing of Soil Moisture with Microwave Radiometry. In Proceedings of the 2008 IEEE International Geoscience and Remote Sensing Symposium, Boston, MA, USA, 7–11 July 2008; pp. II-695–II-698.
49. Mätzler, C.; Wiesmann, A. Documentation for MEMLS, Version 3 ‘Microwave Emission Model of Layered Snowpacks’. MEMLS Manual, Version: 04.05.12. 2012. Available online: <http://www.iap.unibe.ch/publications/pub-detail.php?lang=de&id=236> (accessed on 17 November 2017).
50. Hallikainen, M.; Ulaby, F.; Dobson, M.; El-Rayes, M. Dielectric measurements of soils in the 3- to 37-GHz band between  $-50^{\circ}\text{C}$  and  $23^{\circ}\text{C}$ . In Proceedings of the IGARSS’84: Remote Sensing, from Research Towards Operational Use, Strasbourg, France, 27–30 August 1984.
51. Liebe, H.J.; Hufford, G.A.; Manabe, T. A model for the complex permittivity of water at frequencies below 1 THz. *Int. J. Infrared Millim. Waves* **1991**, *12*, 659–675. [[CrossRef](#)]

52. Wigneron, J.-P.; Jackson, T.; O'Neill, P.; de Lannoy, G.; de Rosnay, P.; Walker, J.; Ferrazzoli, P.; Mironov, V.; Bircher, S.; Grant, J. Modelling the passive microwave signature from land surfaces: A review of recent results and application to the L-band SMOS & SMAP soil moisture retrieval algorithms. *Remote Sens. Environ.* **2017**, *192*, 238–262.
53. Kerr, Y.H.; Waldteufel, P.; Richaume, P.; Wigneron, J.P.; Ferrazzoli, P.; Mahmoodi, A.; Al Bitar, A.; Cabot, F.; Gruhier, C.; Juglea, S.E.; et al. The SMOS Soil Moisture Retrieval Algorithm. *IEEE Trans. Geosci. Remote Sens.* **2012**, *50*, 1384–1403.
54. Entekhabi, D.; Njoku, E.G.; Neill, P.E.O.; Kellogg, K.H.; Crow, W.T.; Edelstein, W.N.; Entin, J.K.; Goodman, S.D.; Jackson, T.J.; Johnson, J.; et al. The Soil Moisture Active Passive (SMAP) Mission. *Proc. IEEE* **2010**, *98*, 704–716. [[CrossRef](#)]



© 2017 by the authors. Licensee MDPI, Basel, Switzerland. This article is an open access article distributed under the terms and conditions of the Creative Commons Attribution (CC BY) license (<http://creativecommons.org/licenses/by/4.0/>).